

Physics-Based Iterative Reconstruction for Dual Source and Flying Focal Spot Computed Tomography

Xiao Wang

Computational Radiology Laboratory, Department of Radiology, Boston Childrens Hospital,
Harvard Medical School, Boston, Massachusetts 02115

Robert D. MacDougall

CT Medical Affairs, Canon Medical Systems USA, Tustin, California 92780

Charles A. Bouman

School of Electrical and Computer Engineering, Purdue University, West Lafayette, Indiana
47907

Simon K. Warfield

Computational Radiology Laboratory, Department of Radiology, Boston Childrens Hospital,
Harvard Medical School, Boston, Massachusetts 02115

Abstract

Purpose: For single source medical Computed Tomography (CT), both Filtered-Back Projection (FBP) and statistical iterative reconstruction have been investigated. However for dual source CT with flying focal spot (DS-FFS CT), iterative reconstruction techniques that accurately model the scanner geometry and acquisition physics have remained unexplored. Therefore, our purpose is to present a novel physics based iterative reconstruction method for DS-FFS CT and assess its image quality.

Methods: Our algorithm uses novel physics models to reconstruct from the native cone-beam geometry and interleaved dual source helical trajectory of a DS-FFS CT. To do so, we construct a noise physics model to represent data acquisition noise and a prior image model to represent image noise and texture. In addition, we design forward geometry physics models to compute the locations for deflected focal spots, the dimension and sensitivity for voxels and detector units, as well as the length of intersection between X-rays and voxels. The forward geometry models further represent the coordinated movement between the dual sources by computing their X-ray coverage gaps and overlaps at an arbitrary helical pitch. With the above models, we reconstruct images by using an advanced Consensus Equilibrium (CE) numerical method to compute the *maximum a posteriori* estimate to a joint optimization problem that simultaneously fits all models.

Results: We compared our reconstruction with the FBP and the Penalized Weighted Least Squares (PWLS) methods in terms of spatial resolution, noise profile and image artifacts on CT ACR phantom as well as clinical datasets. Experiments show that our reconstruction has a higher spatial resolution, with a Modulation Transfer Function (MTF) 3.2 times higher than FBP at spatial frequency 0.8 mm^{-1} . In addition, our reconstruction shows a reduced magnitude of image artifacts compared to FBP and PWLS on all datasets, especially for scans with a high helical pitch.

Conclusions: By modeling a precise geometry and avoiding data rebinning, completion or interpolation, our physics based reconstruction achieves a higher spatial resolution and much fewer image artifacts with smaller magnitude than FBP and PWLS.

Keywords: Dual Source CT, Flying Focal Spot, PWLS, Iterative Reconstruction.

I. Introduction

Dual source computed tomography (CT) is a popular imaging modality that mounts two X-ray sources and detectors on the same rotating gantry, and uses a high helical pitch to rapidly acquire projections with high temporal resolution. With a dual source CT design, radiologists can examine heart and coronary arteries with much fewer motion artifacts than the single source design that has few detector rows¹. In addition, patients who have trouble holding still on a patient bed, such as children and patients with neurological disorders, are less likely to require anesthesia when being scanned by a dual source CT, thereby reducing the exam cost and sedation medical risks².

A high helical pitch for dual source scanner, however, reduces sampling rate and in turn causes a degraded spatial resolution and more undersampling artifacts. To maintain spatial resolution and minimize artifacts, there are two approaches among CT vendors to increase sampling rate while keeping a high pitch. The first approach is to increase the CT detector resolution so that each projection has more samples. An example is the Aquilion Precision Scanner of Canon with 0.25 mm detector resolution and a small field-of-view. The Aquilion Precision Scanner, however, is not in clinical use and its diagnostic accuracy is unknown. The second approach is to increase the total number of projections, such as with the widely used Siemens Somatom Force Scanner. Through the *flying focal spot* (FFS) technology, a dual source scanner takes multiple interleaved projections at each view angle without significantly lengthening the scan time.

To reconstruct from projections at a dual source CT with flying focal spot, abbreviated as DS-FFS CT, both academia and the current clinical practice use the Filtered Back-Projection (FBP) algorithm or its variants. At a high level, FBP reconstruct images by performing the Fourier and inverse Fourier transform to interpolate discretely sampled projections back to a reconstruction in the continuous spatial domain^{3,4}. To save computations, the clinical FBP methods further simplify and approximate the CT geometry by rebinning

Scanner	Clinical FBP	PWLS
Single Source No FFS	Fourier and inverse Fourier Transform Interpolate projections Approximate geometry by rebinning Inferior quality at low dose Inferior quality at large cone angle Popular for clinical practice Short reconstruction time in seconds	Linear Algebra and Bayesian No interpolation No rebinning Preserved quality at low dose Preserved quality at large cone angle Unpopular for clinical practice Much longer reconstruction in hours
Dual Source with FFS	All above features Enable a higher sampling rate than without FFS Enable a much higher pitch than Single Source	No implementation

Table 1: FBP and PWLS algorithmic comparison.

the interpolated helical projections into parallel-beams⁵⁻⁸. With a simplified geometry and reduced computations, FBP has a short reconstruction time and gains wide popularity in practice. Meanwhile, the FBP data interpolation and geometry approximation may negate the image quality advantages from the FFS design and potentially lead to blurry image details as well as unsatisfactory artifacts, especially when the dual source scan cone angle is large and helical pitch is high⁹.

In contrast, statistical iterative reconstruction, such as the Penalized Weighted Least Squares (PWLS) method, is based on linear algebra and Bayesian estimation¹⁰⁻¹⁷ and its algorithmic comparison with FBP is listed in Table 1. PWLS often produces clearer image details with fewer artifacts than FBP, especially when the radiation doses are low, because the PWLS method has more accurate models for data acquisition, sinogram noise and image properties. To further improve spatial resolution, instead of interpolating and rebinning discrete measurements into continuous functions as in FBP, PWLS uses linear algebra to operate directly on discrete measurements and formulates the models as a convex cost function to be minimized^{11,18}. The number of operations for PWLS, however, are several magnitudes more than those for FBP¹⁴. Therefore, PWLS has a slow reconstruction time and is unpopular for clinical practice. In addition to the above disadvantages, the implementation for PWLS is only applicable to single source CT and there is no PWLS implementation for flying focal spot or dual source scanner.

To address these limitations, this paper proposes *The Joint Estimation for Native Geometry* (JENG) algorithm for DS-FFS CT scanner, which accounts for the true acquisition

geometry and jointly estimates images from each X-ray source and focal spot. In Sec. III.B., we propose a novel physics forward model for JENG that imitates the flying focal spot data acquisition and native cone-beam geometry without projection interpolation, rebinning or completion. In Sec. III.C., we characterize and compute the interleaved dual source helical trajectory at a high helical pitch. With precise knowledge of the scanner movement, we then reconstruct images by using Consensus Equilibrium to compute the *maximum a posteriori* estimate to a joint optimization problem that simultaneously fits projections from all focal spots and source-detector pairs. In Sec. V., we evaluated image spatial resolution and artifacts for JENG on a standard ACR 464 phantom dataset with respect to Modulation Transfer Function (MTF), Noise Power Spectrum (NPS) and undersampling artifacts. Experimental results show that JENG has fewer image artifacts and a higher MTF than both FBP and PWLS methods at all spatial frequencies, with an MTF 3.2 times higher than FBP at a spatial frequency of 0.8 mm^{-1} . In the end, we subjectively evaluated the spatial resolution and artifacts for JENG, FBP and PWLS on 5 thoracic datasets and 2 pediatric head scan datasets.

II. Related Work

Flohr and Kachelrieß’s papers analyze focal spot movement on a single source CT, and propose a rebinning FBP method to approximate interleaved helical multislice projection data as progressive-view and parallel-beam data^{7,19}. After the rebinning, a 2D FBP is performed on the rebinned projection data, slice by slice. Such a method has three issues: (1) image blurriness from interpolation and geometry approximation, and the blurriness is often more pronounced in CT datasets with a high pitch and a large CT cone angle²⁰; (2) noticeable aliasing artifacts in image slices and windmill artifacts across image slices in the longitudinal direction; and (3) loss of spatial resolution on the edge of each image slice, as Flohr’s reconstruction is a stack of 2D images rather than a fully 3D volume.

Flohr and his collaborators further extend the above work to DS-FFS CT^{8,21}. As a dual source CT gantry often has limited space to fit two full size detectors, the dual source gantry often has a wide detector covering the full field of view and a narrow detector covering a truncated center view. Therefore, voxels that are located beyond the narrow detector’s truncated field-of-view receive no projections from the narrow detector, despite that these

voxels still receive projections from the wide detector. To perform reconstruction on these voxels with limited projections, Flohr’s research work completes the missing projections from the narrow detector by interpolating projections from the wide detector. Then, the final reconstruction is the weighted average of the two independent FBP reconstructions performed on the completed projections from the two detectors⁸. Such an approach not only has the same issues from the single source CT as discussed in the previous paragraph, but can also lead to more image blurriness and artifacts from missing data interpolation and weighted averaging on independent reconstructions.

In contrast, PWLS reconstructs from projections by precisely modeling the CT geometry, sinogram noise and image spatial property, and using linear algebra to combine these models together as an optimization problem¹¹. Since PWLS does not involve Fourier or inverse Fourier transform and uses precise physics-geometry models, PWLS has fewer interpolation and geometry approximation artifacts than FBP methods despite at a much higher computational cost. In addition, PWLS produces a truly 3D reconstruction and can show more features in the longitudinal direction than the FBP methods. The state-of-the-art PWLS, however, is only applicable to single source CT without flying focal spot, and it is unknown how PWLS can be applied to DS-FFS CT and merge individual reconstructions from two sources into a consensus solution without projection completion.

To address the above mentioned issues, this paper proposes the JENG algorithm, which is the first physics based iterative reconstruction solution for DS-FFS CT and reconstructs from the scanner native geometry without data rebinning, interpolation or completion. Thereby, the images reconstructed by JENG have a higher spatial resolution and fewer image artifacts than both the FBP and the PWLS methods. In addition, to avoid potential image artifacts from weighted averaging on two independent reconstructions as in the FBP methods^{8,21}, the JENG algorithm uses Consensus Equilibrium to compute a single reconstruction that simultaneously fits the projections from all X-ray sources and focal spots.

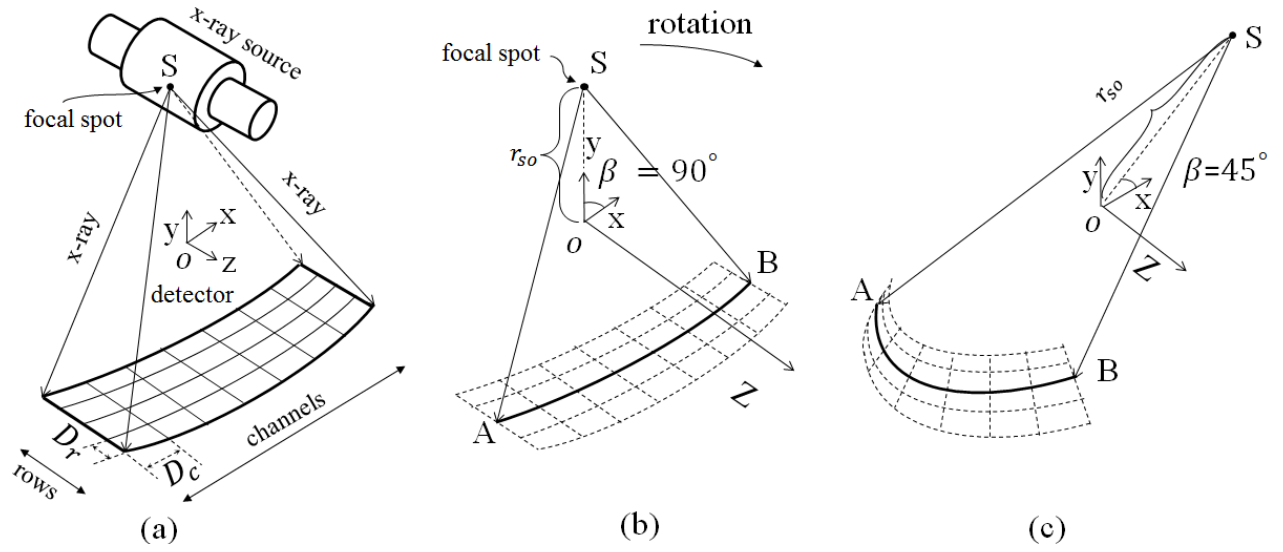


Figure 1: Single source CT scanner geometry and setup. (a) and (b) single source CT scanner at 90° view angle, where S, O and β are the focal spot, isocenter and view angle. (c) CT scanner rotated clock-wise to 45° view angle.

III. Materials and Methods

III.A. CT Setup and Math Formulation

Fig. 1(a) shows a CT scanner with a single X-ray source, also known as an X-ray tube, on one end of a rotating gantry, and an X-ray detector array opposite the source on the gantry. Each horizontal detector sensor unit is a channel and each vertical detector sensor unit is a row. We denote the length of each detector channel as D_c and the length of each detector row as D_r . In addition, the total number of detector channels is M_c and the total number of detector rows is M_r . In the example of Fig. 1(a), the number of detector channels, M_c , is 7 and the number of detector rows, M_r , is 4. The center of the gantry rotation, known as the isocenter, is denoted as point O in Fig. 1(a). For ease of understanding, we use a coordinate system with axis x pointing along the detector channel direction, axis y pointing upright (together x-y form the trans-axial plane), and axis z pointing along the rotation axis (axial plane). The center of the patient body to be scanned is placed near the isocenter O and the cranio-caudal direction is along the z axis. X-rays emit from a point in the X-ray source, also known as a focal spot and is denoted as S in Fig. 1(a), penetrate through the patient body and project onto the X-ray detector array. Note that in this paper we symbolize the distance between focal spot, S, and isocenter, O, as r_{so} and is shown in Fig. 1(b). In

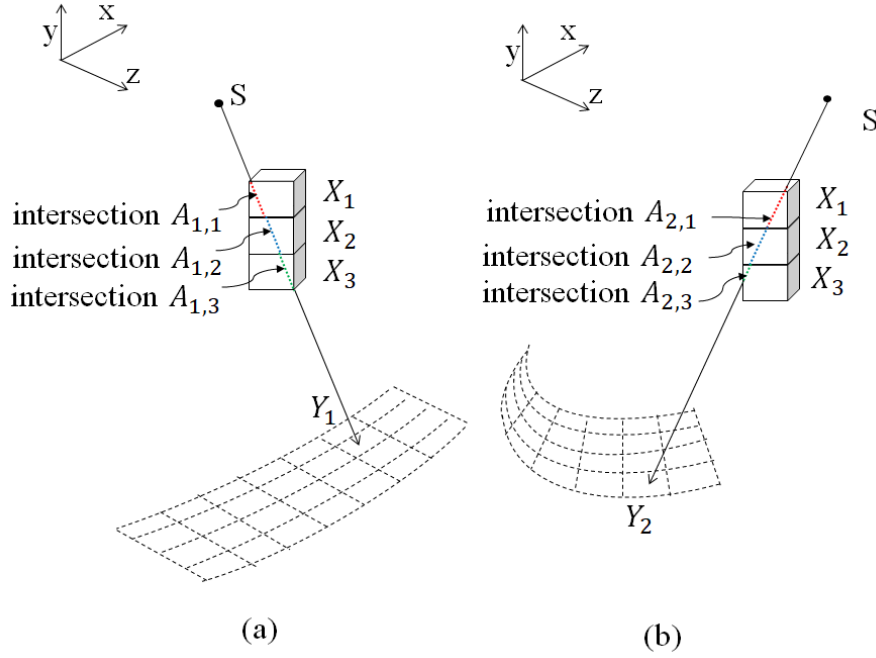


Figure 2: X-rays intersection with voxels at different view angles. (a) At 90° view angle, an X-ray intersects with voxels X_1 , X_2 and X_3 , and we denote the lengths of intersection between the X-ray and the voxels as $A_{1,1}$, $A_{1,2}$, and $A_{1,3}$, respectively. (b) At 45° view angle, a different X-ray intersects with voxels X_1 , X_2 and X_3 with intersection lengths $A_{2,1}$, $A_{2,2}$ and $A_{2,3}$. Note that the length of intersection is unique for each voxel, each X-ray and each view angle.

addition, isocenter, O , is on the same plane with sector SAB , where points A and B are the two end points of the detector center row, shown as a bold arc in Fig. 1(b), and sector SAB is symmetric along line SO . We also define the view angle, β , as the angle between line SO and x axis. In the example of Figs. 1(a) and (b), line SO is along the y axis and the view angle β is 90°. When the CT scanner rotates clock-wise by 45° in Fig. 1(c), the view angle is 45° in this case.

To understand how we formulate the computations for the JENG algorithm, we use a reconstruction with three voxels, X_1 , X_2 and X_3 as an example. Fig. 2(a) shows an X-ray intersecting with three voxels, and a detector sensor unit receives projection Y_1 for the X-ray at 90° view angle. We denote the lengths of intersection for the three voxels at the current view angle as $A_{1,1}$, $A_{1,2}$ and $A_{1,3}$ and we use different colors for each voxel's intersection length. Fig. 2(b) shows another X-ray intersecting with three voxels at 45° view angle with intersection lengths $A_{2,1}$, $A_{2,2}$ and $A_{2,3}$, and a different detector sensor unit takes a projection

Y_2 . Since projections Y_1 and Y_2 are the integral of radiodensity along the path of X-rays, we can express projections Y_1 and Y_2 as: $Y_1 = A_{1,1}X_1 + A_{1,2}X_2 + A_{1,3}X_3 + E_1$, and $Y_2 = A_{2,1}X_1 + A_{2,2}X_2 + A_{2,3}X_3 + E_2$, where X_1 , X_2 and X_3 are the radiodensity for each of the three voxels. E_1 and E_2 are the measurement errors, such as electronic and photon quantum noise, and represent the difference between measured projections, Y_1 and Y_2 , and the error-free perfect projections. If we generalize the above equations for all voxels and projections, then we have:

$$Y = AX + E, \quad (1)$$

In the above equation, Y is a sinogram vector of size M that includes projections from all view angles and M equals $M_v \times M_c \times M_r$, where M_v is the total number of view angles for the scan. M_c and M_r are the number of detector channels and rows as defined before. A is an $M \times N$ system matrix that models the geometry of CT, where N is the size of a reconstruction. Each entry of A , denoted as $A_{i,j}$, represents the length of intersection between j^{th} voxel and the X-ray for the i^{th} sinogram entry. In addition, $A_{i,j}$ is unique for each voxel, detector sensor unit, and view angle. X is a reconstruction vector of size N and each element of X is the radiodensity for a voxel. E is a measurement error vector of size M , and represents the difference between Y and Y 's error-free value. Unfortunately, we cannot directly compute reconstruction X from Eqn. (1) as measurement error E is unknown and cannot be measured. In addition, inverting system matrix A is impractical because an inversion takes huge amount of computations and requires terabytes of memory. To address the above challenges, the JENG algorithm computes reconstruction X as the solution to the following maximum a posteriori optimization problem:

$$X \leftarrow \underset{X}{\operatorname{argmin}} \left\{ \frac{1}{2}(Y - AX)^T D(Y - AX) + R(X) \right\}, \quad (2)$$

where D is an $M \times M$ diagonal weight matrix and represents the inverse of the sinogram noise. $\frac{1}{2}(Y - AX)^T D(Y - AX)$ is a forward model that fits reconstruction X with sinogram Y . If reconstruction X has an anomaly, such as metal, the sinogram noise will be large and the forward model will be penalized with a small weight matrix D . Therefore, reconstruction X has a weak fitting with beam hardened and noisy sinogram Y and has less image noise or artifacts. Vice versa if the sinogram noise is small, the weight matrix D is large and

reconstruction X has a strong fitting with noiseless sinogram Y . $R(X)$ in Eqn. (2) is a prior model for maintaining a good image spatial property and denoising. In this paper $R(X)$ is a convex Generalized Markov Random Field, which denoises and penalizes each voxel based on the difference between the voxel and its neighboring voxels. A large difference leads to a strong denoising and penalization, while a small difference leads to a weak denoising and penalization. From the machine learning perspective, the forward model can be understood as the minimum mean square error of a weighted linear regression model, and $R(X)$ is a regularizer that prevents data overfitting.

III.B. Flying Focal Spot Geometry Modeling

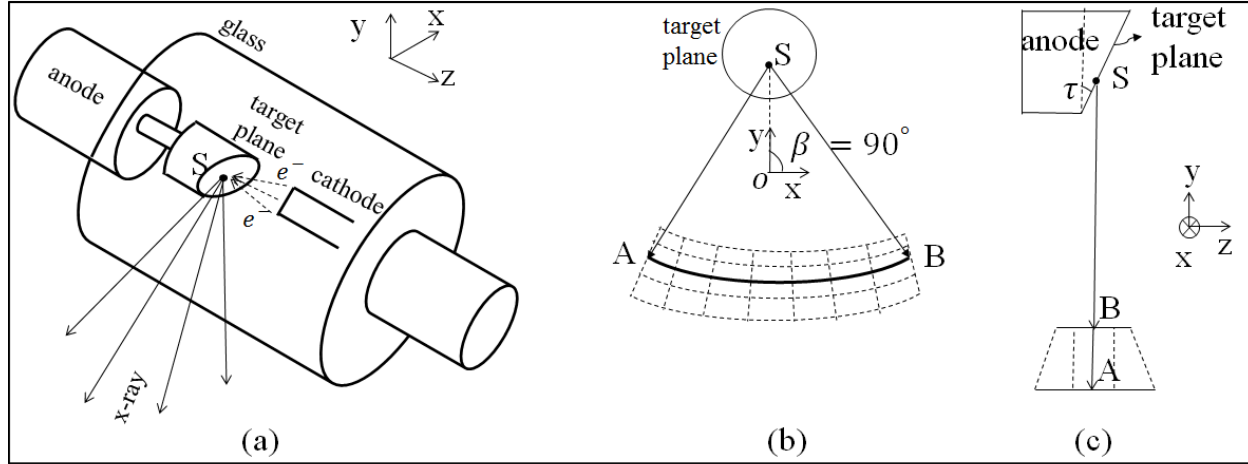


Figure 3: An X-ray source without flying focal spot. (a) Demonstrates the interior design of an X-ray source. Note that the anode target plane is tilted along the z axis. (b) The transverse view (axial plane perspective) for the focal spot and the detector at 90° view angle. (c) The side view (sagittal plane perspective) for the focal spot and the detector.

To compute system matrix A in Eqn. (2), we start by examining the structure inside the X-ray source through Fig. 3(a). The X-ray source consists of an encapsulating glass envelope, a rotating anode, a cathode and a tilted target plane. The target plane is also connected with the anode and is tilted from the X-Y plane by an anode tilt angle τ . From the cathode, the accelerated electrons, denoted as e^- in Fig. 3(a), hit the focal spot S on the anode target plane and the X-rays are then produced at the focal spot. Figs. 3(b) and (c) show the X-ray source structure at 90° view angle from transverse view (axial plane) perspective and side view (sagittal plane) perspective and we can observe that focal spot S lies on the tilted

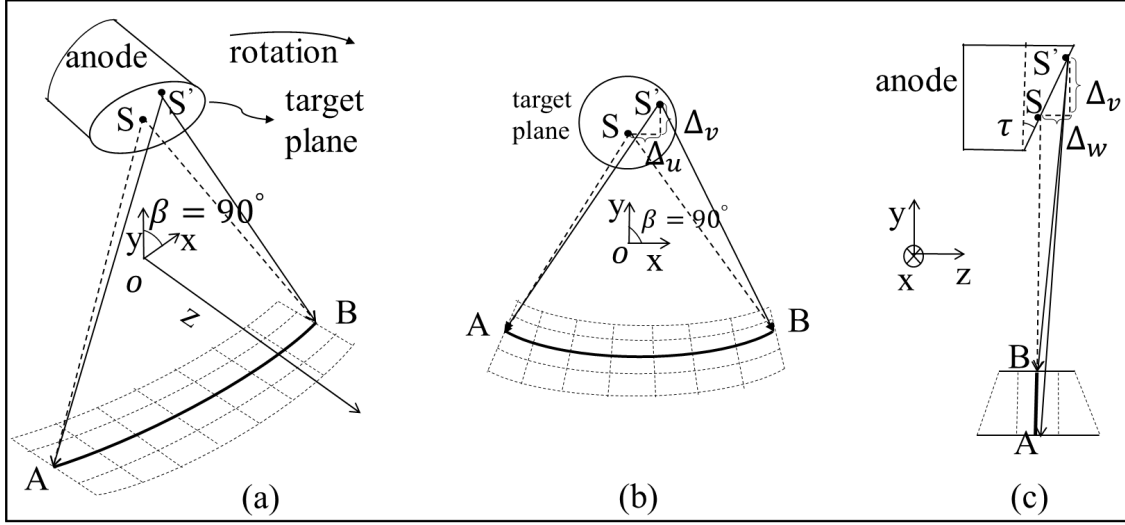


Figure 4: An X-ray source with flying focal spots. (a) Shows a single source CT setup with two focal spots, S and S'. (b) Shows the axial plane transverse view of the focal spots at 90° view angle. (c) The saggital plane side view of the focal spots. Note that S and S' are on the same tilted target plane.

target plane. Fig. 3(c) also shows the anode angle τ as the angle between y axis and the tilted target plane. Furthermore to the above introduction, the precise coordinate location (x_s, y_s, z_s) for focal spot S at any view angle β can be computed as:

$$x_s = r_{so} \cos(\beta), \quad \text{and} \quad y_s = r_{so} \sin(\beta), \quad \text{and} \quad z_s = \frac{H_r(\beta - \beta_0)}{2\pi}, \quad (3)$$

where the cosine and sine trigonometry relationship for x_s and y_s can be observed in Fig. 1(c). H_r is how far the X-ray source moves along the z axis in a 360° rotation, β is the view angle in radian, and β_0 is the CT scanner view angle when $z_s = 0$.

When the scanner is equipped with flying focal spot, the cathode quickly wobbles and electrons hit the target plane at multiple different locations, creating multiple X-ray focal spots at each view angle. Each focal spot produces a set of projections and different focal spots produce different but interleaved projections. By producing conjugate sets of projections through flying focal spots, the total number of projections, M , increases proportionally with the number of focal spots but the CT scan time does not significantly lengthen. Fig. 4(a) shows an example single source CT scanner with two focal spots, the default focal spot S and the deflected focal spot S', and Figs. 4(b) and (c) show S and S' in the axial and saggital plane perspectives at 90° view angle. We can observe from Figs. 4(a) and (b) that projections from S and S' overlap but do not contain each other.

To compute the coordinate location for flying focal spot, we denote the displacement vector between S and S' at 90° view angle as $(\Delta_u, \Delta_v, \Delta_w)$ in Figs. 4(b) and (c). Since focal spots S and S' are on the same target plane, Δ_v and Δ_w have the following trigonometry relationship: $\Delta_w = \tan(\tau)\Delta_v$, where τ is the anode tilt angle. The deflected focal spot, S', at any view angle β can then be given below with coordinate (x'_s, y'_s, z'_s) :

$$\begin{bmatrix} x'_s \\ y'_s \\ z'_s \end{bmatrix} = \begin{bmatrix} r_{so} \cos(\beta) \\ r_{so} \sin(\beta) \\ \frac{H_r(\beta-\beta_0)}{2\pi} \end{bmatrix} + R_\beta \begin{bmatrix} \Delta_u \\ \Delta_v \\ \tan(\tau)\Delta_v \end{bmatrix}, \quad \text{and} \quad R_\beta = \begin{bmatrix} \sin(\beta) & \cos(\beta) & 0 \\ -\cos(\beta) & \sin(\beta) & 0 \\ 0 & 0 & 1 \end{bmatrix}, \quad (4)$$

where the vector before the addition operator is the coordinate location for the default focal spot from Eqn. (3). R_β is a rotation matrix that rotates the displacement between S' and S at 90° view angle to any view angle, β , assuming that a helical CT scanner rotates in the x-y plane and translates in the z direction. After plugging in the R_β expression, Eqn. (4) can be reorganized as:

$$\begin{bmatrix} x'_s \\ y'_s \\ z'_s \end{bmatrix} = \begin{bmatrix} r_{so} \cos(\beta) + \sin(\beta)\Delta_u + \cos(\beta)\Delta_v \\ r_{so} \sin(\beta) - \cos(\beta)\Delta_u + \sin(\beta)\Delta_v \\ \frac{H_r(\beta-\beta_0)}{2\pi} + \tan(\tau)\Delta_v \end{bmatrix}, \quad (5)$$

Note that Eqn. (5) is a general form for the coordinate location of any focal spot, with or without deflection. If Δ_u and Δ_v are both zeros, then Eqn. (5) is the default focal spot coordinate without deflection and is the same as Eqn. (3). Readers should also know that Eqn. (5) assumes that a focal spot is a sizeless point without actual physical shape. Given that CT scans often use a small focal spot with size less than 1mm for optimal diagnostic values, the focal spot size approximation in Eqn. (5) has minimal or no impact on spatial resolution. In the unusual cases with a focal spot size larger than 1mm, the sizeless point assumption might lead to sub-optimal spatial resolution.

Knowing the coordinate for the focal spots alone, however, is not sufficient to compute system matrix entry, $A_{i,j}$. We also need to know the geometry information for voxel X_j and we introduce two other parameters in this paper, θ and ϕ . θ is voxel X_j 's ray angle in the x-y plane parallel to the x axis, and Fig. 5(a) depicts θ in the x-y plane. Fig. 5(a) also denotes point C as the location where the X-ray hits the detector in the x-y plane. ϕ is the voxel's ray angle in the y-z plane and parallel to the line connecting S' and C, and

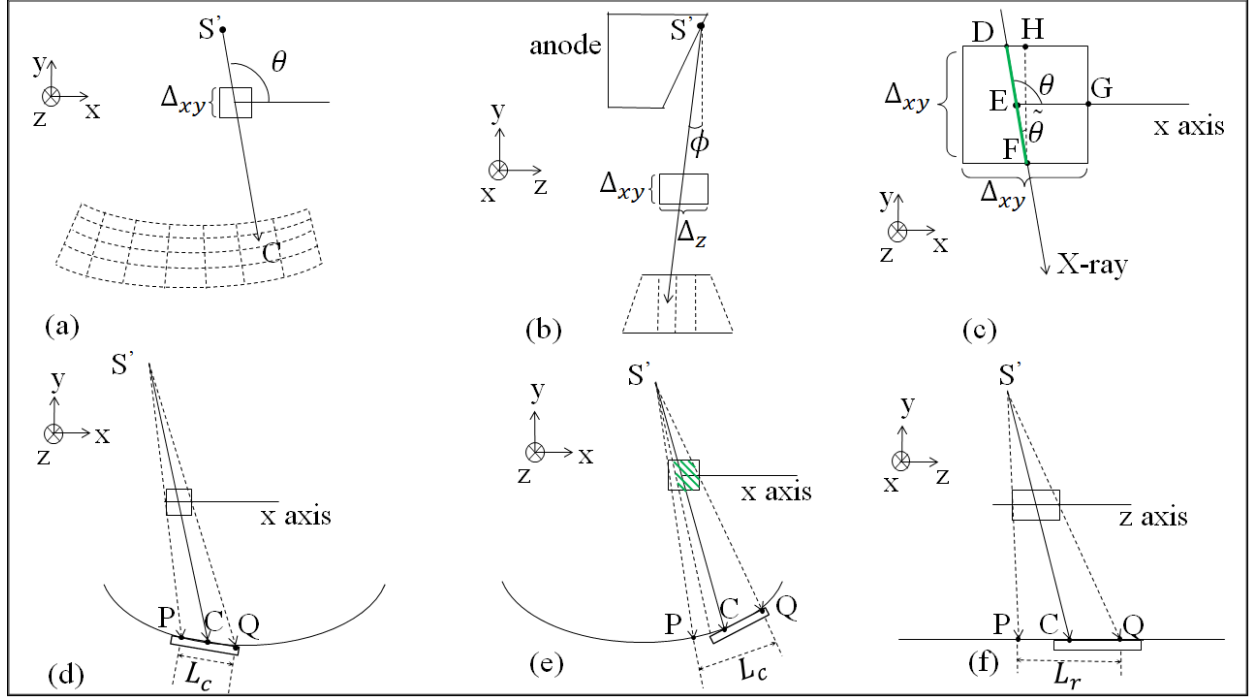


Figure 5: (a) and (b) show x-y plane ray angle θ and y-z plane ray angle ϕ . (c) Green line segment DF is the length of intersection between a voxel and an X-ray that goes through the voxel center. (d) Shows a voxel whose projection onto the detector (x-y plane) is completely within a channel. (e) The voxel's projection partially overlaps with the detector channel. (f) The voxel's projection onto the detector (y-z plane) partially overlaps with a row.

is shown in Fig. 5(b). With the above definition, θ and ϕ can then be computed from the below trigonometry equations:

$$\theta = \arctan2 \left(\frac{y'_s - y_j}{x'_s - x_j} \right), \quad \phi = \arctan2 \left(\frac{z'_s - z_j}{\sqrt{(x'_s - x_j)^2 + (y'_s - y_j)^2}} \right), \quad (6)$$

where $\arctan2$ operator returns the arctangent value in the range of $[-\pi, \pi]$, (x'_s, y'_s, z'_s) is the focal spot coordinate location from Eqn. (5), and (x_j, y_j, z_j) is voxel X_j 's coordinate location. To ensure that the length of intersection, $A_{i,j}$, is never negative, we introduce two more parameters, $\tilde{\theta}$ and $\tilde{\phi}$, which are 45° rotations of θ and ϕ , and we clip their values to $[-\frac{\pi}{4}, \frac{\pi}{4}]$. $\tilde{\theta}$ and $\tilde{\phi}$ are defined below as:

$$\tilde{\theta} = \left[\left(\theta + \frac{\pi}{4} \right) \bmod \frac{\pi}{2} \right] - \frac{\pi}{4}, \quad \tilde{\phi} = \left[\left(\phi + \frac{\pi}{4} \right) \bmod \frac{\pi}{2} \right] - \frac{\pi}{4}, \quad (7)$$

With $\tilde{\theta}$ and $\tilde{\phi}$, the length of intersection, $A_{i,j}$, can then be computed as:

$$A_{i,j} = \frac{\Delta_{xy}}{\cos \tilde{\theta} \cos \tilde{\phi}} \quad (8)$$

In the above equation, we denote a voxel's x-y plane side length as Δ_{xy} and z direction side length as Δ_z in Figs. 5(a) and (b). To explain how Eqn. (8) is derived, Fig. 5(c) shows an X-ray intersecting with voxel X_j and the intersection length, line segment DF, is colored in green. Point E in Fig. 5(c) is the center of the voxel with points D, E, F along the same line. The length of line segment FH equals Δ_{xy} and FH is parallel to y axis with point H on the edge of the voxel. $\angle DEG$ is ray angle θ and $\angle DFH$ is $\tilde{\theta}$, such that θ and $\tilde{\theta}$ are 90° apart in this example. Given that both the length of line segment FH and $\angle DFH$ are known, the length of X-ray's intersection in the x-y plane, segment DF, can be computed as $\frac{\Delta_{xy}}{\cos \tilde{\theta}}$. To project line segment DF from the x-y plane to a three-dimensional space, Eqn. (8) divides DF segment length with $\cos \tilde{\phi}$.

Eqn. (8), however, assumes that a voxel's projection is entirely taken by a single detector sensor unit. When a voxel's projection is taken by multiple detector sensor units, the measurement from any single detector sensor unit, Y_i , can no longer account for the entire voxel's projection. Instead, Y_i is the projection for the portion of the voxel that is in the way of the X-rays from the focal spot to the detector sensor unit that receives Y_i . In the example of Fig. 5(d), the voxel's projection in the x-y plane, shown as line segment PQ in the figure with length L_c , is entirely within a channel. In this example, the projection taken by the detector channel accounts for the entire voxel and the computations for Eqn. (8) is accurate. In another example in Fig. 5(e), the voxel is partially in the way of the X-rays and its projection in the x-y plane, namely line segment PQ, does not fully overlap with the detector channel. In such an example, the projection taken by the channel only accounts for the portion of the voxel shaded in green and Eqn. (8) no longer holds. Similarly, Fig. 5(f) gives an example voxel whose projection in the y-z plane, line segment PQ with length L_r , does not fully overlap with the detector row.

Therefore, $A_{i,j}$ in Eqn. (8) must be modified so that $A_{i,j}$ not only reflects the length of intersection between X-rays and voxels, but also reflects the overlap between the voxel's projection and the corresponding detector sensor unit. To do so, $A_{i,j}$ is multiplied by a

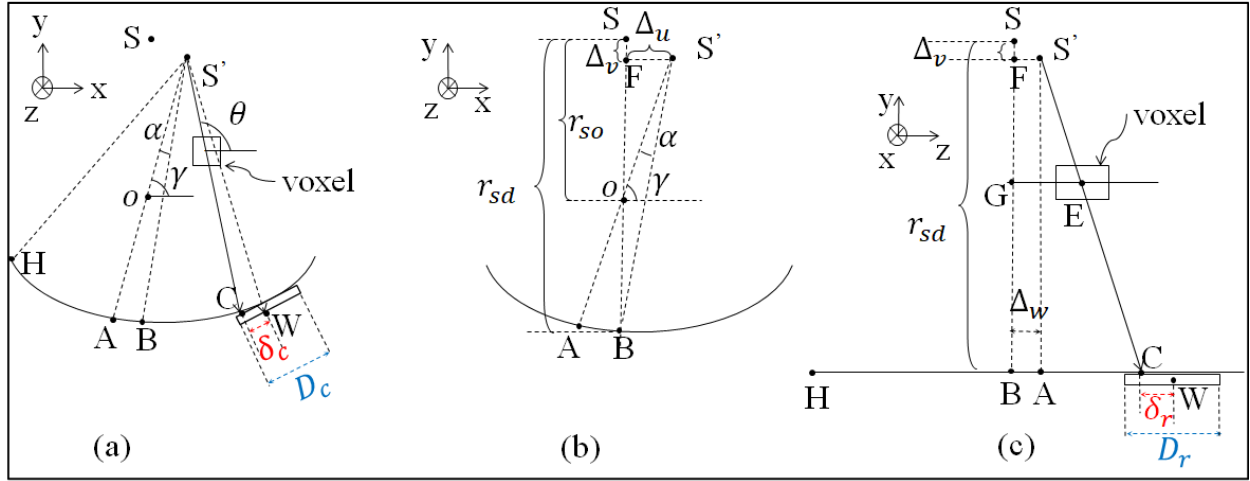


Figure 6: (a) and (b) demonstrate how δ_c is computed, with δ_c colored as a red segment between points C and W. (c) Shows how δ_r is computed. Similar to (a), δ_r is red segment CW.

normalization term and is computed in the following way:

$$A_{ij} = \frac{\Delta_{xy}}{\cos \theta \cos \phi} [V(\delta_c) * W(\delta_c)] \times [V(\delta_r) * W(\delta_r)] , \quad (9)$$

where δ_c is the x-y plane displacement between the center of voxel X_j 's projection and the center of the channel that receives projection Y_i . δ_r is the y-z plane displacement between the center of the voxel's projection and the center of the detector row. Figs. 6(a), (b) and (c) depict δ_c and δ_r as red segments CW, where point C is the center of the voxel's projection and point W is the center of the corresponding detector sensor unit.

In addition to the above notations, $V(\cdot)$ in Eqn. (9) is a voxel density function and $W(\cdot)$ is a detector sensitivity function. $*$ is a convolution operation and \times is a multiplication operation. $\frac{\Delta_{xy}}{\cos \theta \cos \phi}$ computes the length of intersection between the X-ray and voxel X_j , as explained in Eqn. (8), whereas $[V(\delta_c) * W(\delta_c)] \times [V(\delta_r) * W(\delta_r)]$ is a normalization term that accounts for the overlap between voxel X_j 's projection and the detector sensor unit that receives the projection. $V(\delta_c) * W(\delta_c)$ accounts for the x-y plane overlap and $V(\delta_r) * W(\delta_r)$ accounts for the y-z plane overlap. When a voxel's projection completely overlaps with a detector sensor unit, such as in the example of Fig. 5(d), the normalization term is 1. Otherwise, the normalization term is between 0 and 1. To define $V(\delta_c)$, $V(\delta_r)$, $W(\delta_c)$, and $W(\delta_r)$, we assume that each voxel has a uniform radiodensity everywhere in the voxel and each detector sensor unit has a uniform sensitivity. For simplicity, we borrow the voxel

density and detector sensitivity functions from citation¹¹, and define $V(\cdot)$ and $W(\cdot)$ as the following rectangular functions:

$$V(\delta_c) = \mathbf{rect}\left(\frac{\delta_c}{L_c}\right), \quad \text{and} \quad V(\delta_r) = \mathbf{rect}\left(\frac{\delta_r}{L_r}\right) \quad (10)$$

$$W(\delta_c) = \frac{1}{D_c} \mathbf{rect}\left(\frac{\delta_c}{L_c}\right), \quad \text{and} \quad W(\delta_r) = \frac{1}{D_r} \mathbf{rect}\left(\frac{\delta_r}{L_r}\right) \quad (11)$$

where L_c and L_r , as defined before, are the lengths of the voxel's projection in the x-y plane and y-z plane, and are represented as line segment PQ in Figs. 5(d), (e) and (f). D_c and D_r are the lengths for a detector channel and row, respectively, and are colored as blue line segments in Figs. 6(a) and (c). After plugging Eqns. (10) and (11) into Eqn. (9), we eliminate the convolution operations and rewrite Eqn. (9) in a closed-form expression:

$$A_{ij} = \frac{\Delta_{xy}}{D_c D_r \cos \tilde{\theta} \cos \tilde{\phi}} \mathbf{clip}\left[0, \frac{D_c + L_c}{2} - |\delta_c|, \min(L_c, D_c)\right] \times \mathbf{clip}\left[0, \frac{D_r + L_r}{2} - |\delta_r|, \min(L_r, D_r)\right], \quad (12)$$

with function **clip** defined as: $\mathbf{clip}[a, b, c] = \min(\max(a, b), c)$. To compute $A_{i,j}$ correctly, δ_c and δ_r in the above equation must compensate for the flying focal spot deflection. The value for δ_c is clipped to $[-(r_{sd} + \Delta_v)\pi, (r_{sd} + \Delta_v)\pi)$ and can be computed as:

$$\delta_c \approx \left[\left(\theta - \gamma - \alpha + \frac{(M_c - 1)D_c}{2(r_{sd} + \Delta_v)} - \frac{i_c D_c}{r_{sd} + \Delta_v} + \pi \right) \bmod 2\pi - \pi \right] (r_{sd} + \Delta_v), \quad (13)$$

where γ and α are defined as:

$$\gamma = \beta - \arctan2\left(\frac{\Delta_u}{r_{so} + \Delta_v}\right) \quad (14)$$

$$\alpha = \arctan2\left(\frac{r_{sd} + \Delta_v}{\Delta_u}\right) - \arctan2\left(\frac{r_{so} + \Delta_v}{\Delta_u}\right) \quad (15)$$

In the above equations, θ is the X-ray ray angle in the x-y plane as defined before; γ is the angle between S'O and x axis, and both θ and γ are pointed out in Figs. 6(a) and (b). α is the detector channel offset, defined as the angle between the X-ray hitting the detector center in the x-y plane and the X-ray passing through the isocenter, O. In the example of Figs. 6(a) and (b), α is $\angle AS'B$. Point A is where the X-ray through isocenter O hits the detector array in the x-y plane, and point B is the detector array center in the x-y plane. M_c is the total number of detector channels as defined in Sec. III.A.. r_{so} is the distance from the default focal spot, S, to the isocenter, O. r_{sd} is the vertical distance from S to the detector

array, and both r_{so} and r_{sd} are indicated in Fig. 6(b). Δ_u and Δ_v are the focal spot location displacement, along x axis and y axis respectively, from S to the deflected focal spot, S', and are both indicated in Fig. 6(b). i_c is the index for the detector channel that receives voxel X_j 's projection, and we assume that the index for the leftmost detector channel is zero. In the example of Figs. 6(a) and (b), we use point H to represent the center for the leftmost detector channel and point W for the center of the i_c^{th} channel.

In Eqn. (13), operation $\theta - \gamma$ computes angle $\angle AS'C$ in Fig. 6(a). By subtracting α , which is $\angle AS'B$, the first three terms, $\theta - \gamma - \alpha$, compute $\angle BS'C$. The fourth term, $\frac{(M_c-1)D_c}{2(r_{sd}+\Delta_v)}$, is the approximated angle $\angle HS'B$. Therefore, The result of computing the first four terms in Eqn. (13) is $\angle HS'C$ in the example of Fig. 6(a). The fifth term is the approximated angle $\angle HS'W$. Together, the computations for the first five terms in Eqn. (13) get $\angle CS'W$, which is the angular measure for δ_c , by subtracting $\angle HS'C$ from $\angle HS'W$. Then, Eqn. (13) clips the angle to the range of $[-\pi, \pi)$ and converts from angular measure to arc length at the end of the equation. Similarly, we can compute δ_r as:

$$\delta_r = \frac{r_{sd} + \Delta_v}{\sqrt{(x'_s - x_j)^2 + (y'_s - y_j)^2}}(z_j - z'_s) + \frac{M_r - 1}{2}D_r + \Delta_w - i_r D_r, \quad (16)$$

where (x'_s, y'_s, z'_s) is the coordinate location for a deflected focal spot S' and (x_j, y_j, z_j) is the coordinate location for voxel X_j . M_r is the number of detector rows. Δ_w is the focal spot displacement along z axis from S to S' and is indicated in Fig. 6(c). i_r is the index for the detector row that receives a projection for voxel X_j and we assume that the leftmost row has index 0. In the example of Fig. 6(c), we use point H to indicate the center for the leftmost detector row. The first term in Eqn. (16) computes length AC, where point A is on the detector rows and line S'A is parallel to y axis. The second term computes length HB, where point B is the center of the detector array in the y-z plane. The third term, Δ_w , equals to the length of AB, and the first three terms together compute length HC. The fourth term, $i_r D_r$, computes length HW. In the end, Eqn. (16) computes δ_r by subtracting length HC from length HW.

III.C. Dual Source CT Modeling and Computations

For a dual source CT design, two sources and two detectors at the same X-ray energy level are mounted on a rotating gantry, with each pair of source and detector acquiring conjugate

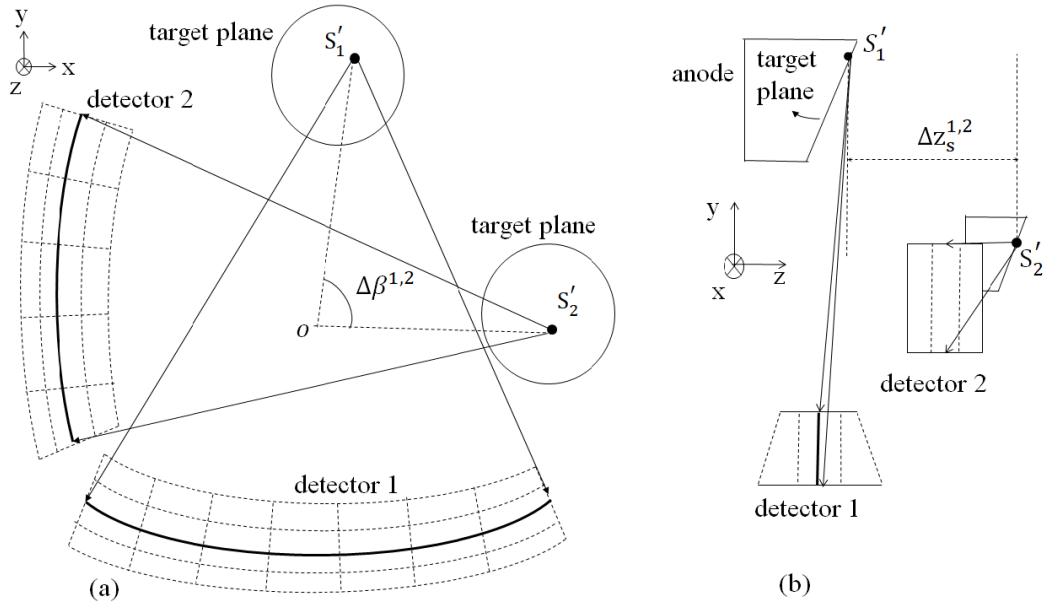


Figure 7: Dual source CT design and geometry. (a) Shows detector 1 of a dual source CT covering the full field of view, and detector 2 covering a smaller and central field of view. In addition, the two detectors are offset by a constant rotation angle, $\Delta\beta^{1,2}$, in the x-y plane. (b) The two detectors are offset by a displacement $\Delta z_s^{1,2}$ in the y-z plane.

but different projections. In addition, different pairs have different geometry parameters with different detector sizes, view angles, and X-ray source movement. Fig. 7(a) shows an example dual source CT. The first X-ray source is S'_1 and its corresponding detector has 7 channels and a large field-of-view. The second X-ray source is S'_2 and its corresponding detector has a smaller size with 5 channels and a smaller field-of-view, given that the rotating gantry has limited space to fit two full size detectors. The focal spot locations between S'_1 and S'_2 are offset by an angular displacement of $\Delta\beta^{1,2}$ in the x-y plane and a translation displacement of $\Delta z_s^{1,2}$ in the z direction. Both $\Delta\beta^{1,2}$ and $\Delta z_s^{1,2}$ are shown in Fig. 7 and $\Delta\beta^{1,2}$ is represented by $\angle S'_1 O S'_2$ in Fig. 7(a). In practice, $\Delta\beta^{1,2}$ is often chosen to be 90° for an efficient mechanical assembly of the detector sensor units.

With the above design, the dual source CT has the unique advantage to enable high pitch scans and rapid data acquisition without significantly increasing undersampling image artifacts. To explain why, Fig. 8 demonstrates the interleaved helical trajectory of a dual source CT. Assuming that the scan has a high pitch, Fig. 8(a) shows detector 1's movement along the z axis across time. Time t_1 , t_2 and t_3 are the 90° view angles from three consecutive rotations when detector 1 and its source are in an upright position. In addition, it takes

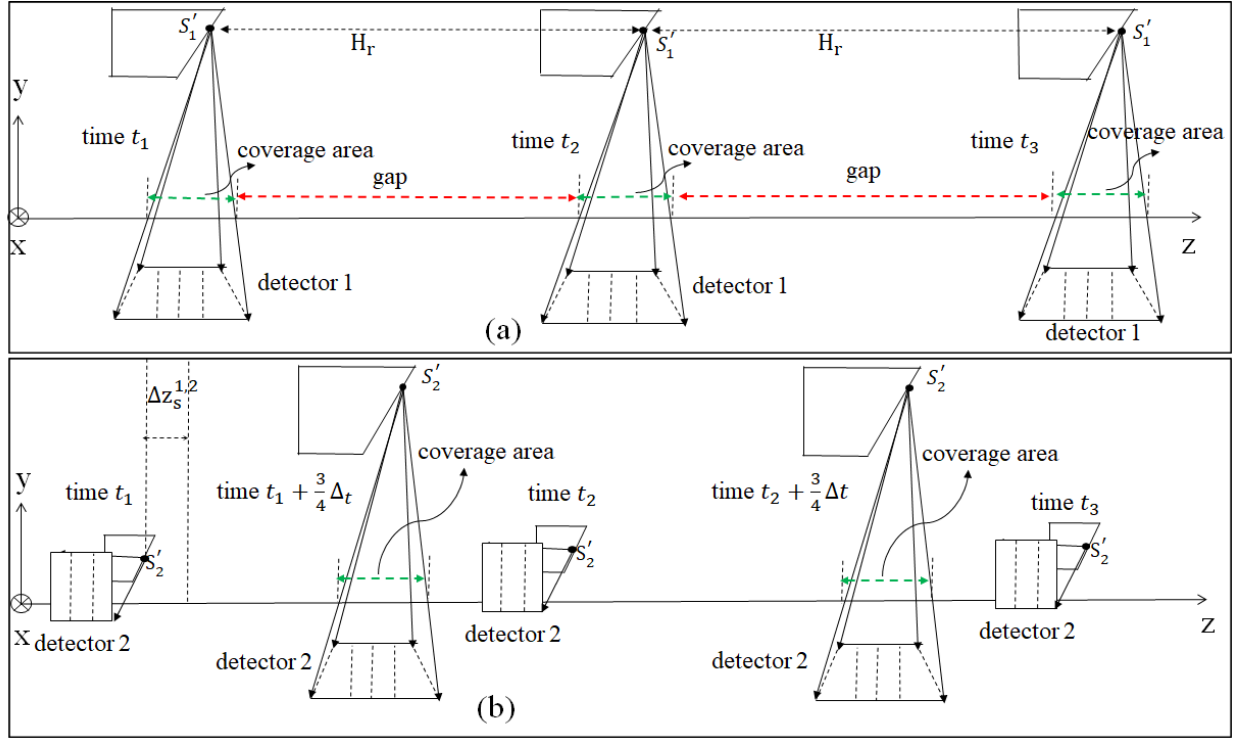


Figure 8: Demonstrates the dual sources' coordinated movement and shows their X-ray coverage gaps and overlaps. (a) Dual Source CT detector 1's movement in the z direction across time. Time t_1 , t_2 and t_3 are three consecutive rotations. Note that the gaps between consecutive rotations are much larger than the X-ray coverage areas. (b) Detector 2's z axis movement at time t_1 , t_2 and t_3 . Note that detector 2's X-ray coverage areas partially fill the coverage gaps of detector 1.

exactly Δ_t seconds and a distance of H_r for the X-ray source to move from its location at time t_1 to t_2 or t_2 to t_3 , where H_r is the rotation distance and was defined before in Eqn. (3). At 90° view angles, the areas of the patient body covered by X-rays are marked by green line segments. Meanwhile, the high pitch scan leads to X-ray coverage gaps between consecutive rotations, shown as red line segments in the figure, and the gaps are not covered by any X-rays at 90° view angles. Consequently, a reconstruction from detector 1's projections alone will lead to unacceptable image quality with significant undersampling artifacts. To reduce the artifacts, detector 2 and its source are designed to provide extra X-rays coverage that diminishes the coverage gaps of detector 1 and increases the number of projection samplings. In Fig. 8(b), detector 2 and its source have a 90° angular displacement from detector 1 and lie horizontally at time t_1 . In addition, detector 2 have a z direction translation displacement of $\Delta z_s^{1,2}$ from detector 1. From time t_1 , it takes detector 2 and its source exactly $\frac{3}{4}\Delta_t$ seconds to rotate to an upright position. In the example of Fig. 8(b), we note that along the z axis,

detector 2 at time $t_1 + \frac{3}{4}\Delta_t$ is located between the positions for detector 1 at time t_1 and t_2 . Therefore, the X-ray coverage for detector 2 partially fills the gaps of detector 1 and provides the missing projections for detector 1 in areas where no X-rays is available. With the additional projections from detector 2, a dual source CT thereby minimizes the increase in high pitch undersampling artifacts.

Despite of the benefits above, we can observe from Fig. 8 that the additional projections from detector 2 do not completely fill the X-rays coverage gaps of detector 1. Therefore, a high pitch dual source CT can still lead to noticeable undersampling artifacts in reconstructed images due to the projection undersampling. To make it even worse, the state-of-the-art FBP methods for dual source CT heavily utilize data interpolation and geometry approximation, leading to even more pronounced undersampling artifacts^{8,21}. In response, this section proposes a joint estimation framework for JENG that has no data interpolation and the reconstruction simultaneously fits projections and geometry from both source-detector pairs. Consequently, JENG can better take advantage of the dual source CT design for more effective artifacts reduction than FBP. To implement the JENG algorithm, we construct the system matrices A^1 and A^2 for the first and the second source-detector pairs by following the system matrix computations in Eqn. (12). Then, the following joint estimation cost function finds a consensus solution that fits projections and geometry for both source-detector pairs:

$$X \leftarrow \underset{X}{\operatorname{argmin}} \left\{ \frac{1}{2} \|Y^1 - A^1 X\|_{D^1}^2 + \frac{1}{2} \|Y^2 - A^2 X\|_{D^2}^2 + R(X) \right\}, \quad (17)$$

where Y^1 , A^1 , and D^1 are the sinogram projections, system matrix and weight matrix for the first source-detector pair, and Y^2 , A^2 , and D^2 are those for the second pair. X is a consensus reconstruction that fits geometries and projections from both pairs. $\|Y^1 - A^1 X\|_{D^1}^2$ is a short-hand notation for vector norm $(Y^1 - A^1 X)^T D^1 (Y^1 - A^1 X)$. Similarly, the same notation is applied to $\|Y^2 - A^2 X\|_{D^2}^2$.

To consider cases when each source-detector pair has multiple flying focal spots, we construct an independent system matrix for each focal spot at each source-detector pair. For example, if a dual source CT has four focal spots at each source-detector pair, then we have eight system matrices in total. In a general case with K system matrices, the joint

estimation cost function has the following form:

$$X \leftarrow \operatorname{argmin}_X \left\{ \frac{1}{2} \sum_{k=1}^K \|Y^k - A^k X\|_{D^k}^2 + R(X) \right\}, \quad (18)$$

where K is the total number of system matrices that equals to the number of source-detector pairs multiplied by the number of focal spots, and k is the index for k^{th} system matrix and forward model. Y^k , D^k are the projections and weight matrix corresponding to the k^{th} system matrix.

As all forward and prior models in the above equation are strictly convex, there exists a unique global minimum to Eqn. (18). A wide variety of numerical methods can be used to compute the global minimum of the above cost function, including Iterative Coordinate Descent^{14,22–24}, Gradient Descent, and Conjugate Gradient Descent²⁵. Unfortunately no matter which numerical method to use, all methods have trouble with storing the system matrices in memory as the system matrices have a very large memory requirement and their memory size is proportional to both the reconstruction size, N , and the measurements size, M . For a large-scale reconstruction, the system matrices can sometimes take hundreds of terabytes of memory, which is beyond what a standard computer workstation can possibly provide¹⁸.

To lower the memory requirement, there exists two approaches: (1) the ordered-subsets method^{26,27}, and (2) the on-the-fly method²⁸. The ordered-subsets method splits measurements and the system matrices into subsets and distributes them among compute nodes. Therefore, the memory requirement for each node is the assigned subset only. Each node then computes a private reconstruction using its assigned subset and merges the private reconstructions from all nodes into a consensus solution. The ordered subsets method, however, is an approximation method and a convergence to the global minimum to Eqn. (18) is not guaranteed²⁶. If measurements are uniformly sampled among subsets, the ordered-subset method converges to a value close to the global minimum. If measurements are partitioned non-uniformly, the converged solution is far from the global minimum. In contrast, the on-the-fly method divides voxels into small groups and updating all groups in sequence. At each voxel group, the on-the-fly method computes and stores a small portion of the system matrices that are needed by the current group. Once the on-the-fly method finishes the update for the current group and moves on to the next one, the previous memory storage

is emptied and a new portion of the system matrices for the next voxel group are computed and stored in memory. Despite that the on-the-fly method has little memory requirement, the on-the-fly method significantly increases the computation cost and reconstruction time because the on-the-fly method recomputes the entire system matrices in every iteration of the numerical method.

Recently, a new numerical method, Consensus Equilibrium (CE), partitions the system matrices and measurements across nodes in any order, including any non-uniform sampling^{18,29,30}. Then each node computes an individual reconstruction from its assigned subset and merges individual reconstructions into a consensus solution that is provably exactly the global minimum to Eqn. (18). Therefore unlike the ordered-subsets approximation method, CE is a precise method and convergence is guaranteed for any partition. In addition, the CE Method pre-computes and stores partitioned system matrices and measurements in the memory of each node. Therefore, the CE Method avoids problems such as repeated computations and reconstruction time increase that are prevalent for the on-the-fly method. Although the CE Method has clear advantages over both the ordered-subsets and the on-the-fly method, the CE Method has not been used for DS-FFS CT iterative reconstruction and this section discusses how the CE Method is used for such purpose for the first time.

To understand the CE Method, we use notation V^k for the individual reconstruction that fits projection subset Y^k and system matrix subset A^k . Then the CE Method's proximal function, denoted as $F_k(X)$ and defined below, finds a balance between individual reconstruction, V^k , and the consensus solution, X :

$$V^k \leftarrow \operatorname{argmin}_{V^k} F_k(X) = \operatorname{argmin}_{V^k} \left\{ \frac{1}{2} \|Y^k - A^k V^k\|_{D^k}^2 + \frac{R(V^k)}{K} + \frac{\|V^k - X\|^2}{2\sigma^2} \right\}, \quad (19)$$

where the first two terms for $F_k(X)$ fit the individual reconstruction, V^k , with the k^{th} forward model and the prior model. The third term, $\frac{\|V^k - X\|^2}{2\sigma^2}$, penalizes the difference between the individual reconstruction, V^k , and the consensus solution, X . σ controls the convergence rate and the best σ for convergence is determined experimentally. In every iteration of the CE method, each node evaluates Eqn. (19), computes the system matrix for the k^{th} forward model in Eqn. (18), and produces an individual solution, V^k . Then, individual reconstructions from all nodes are fused together for an updated consensus solution, X . If the new consensus solution, X , is different from individual reconstruction, V^k , then iterations

repeat until $X = V^k$, where k is from 1 to K . Otherwise, the consensus solution X is the global minimum to Eqn. (18). Since the CE Method is not a theoretical contribution of this paper but a new application to DS-FFS CT reconstruction, we succinctly summarize the CE Method and its fusing operation in the following framework:

1. For each forward model k from 1 to K , we introduce a variable U^k as an input change to the proximal map function and is initialized to equal V^k . In addition, we introduce W^k , which is a temporary copy of V^k .
2. While individual reconstructions V^1, V^2, \dots, V^K are not equal, we repeatedly do the following steps to each proximal map function and individual reconstruction:
 - (a) Compute individual reconstruction, $V^k \leftarrow \operatorname{argmin}_{V^k} F_k(X + U^k)$.
 - (b) Store a copy of W^k as $(W')^k$.
 - (c) Compute $W^k \leftarrow 2V^k - X - U^k$.
 - (d) Update $W^k \leftarrow \rho W^k + (1 - \rho)(W')^k$, where ρ is a convergence parameter and is chosen to be between 0 and 1.
 - (e) $X \leftarrow \left(\sum_{k=1}^K W^k \right) / K$, so that the consensus solution X is updated to be the arithmetic mean of W^1, W^2, \dots, W^K .
 - (f) The proximal map function input change, U^k , is updated to be $U^k \leftarrow X - W^k$.

In the above framework, step 2a updates each individual reconstruction by computing their proximal map functions. Steps 2b to 2f fuse the individual reconstructions into a consensus solution, X . If X does not equal to all individual reconstructions, the framework repeats.

IV. Experiment Setup

We acquired data from a dual source Siemens Somatom Force CT scanner to assess the performance of the algorithms. The Siemens Force Scanner at its default focal spot location has a 595 mm source-to-isocenter distance ($r_{so} = 595$ mm), and a 1085.6 mm source-to-detector distance ($r_{sd} = 1085.6$ mm). Detector sensor units are formed on an arc concentric to the X-ray source. At the single source mode, the CT detector has 96 rows and 920

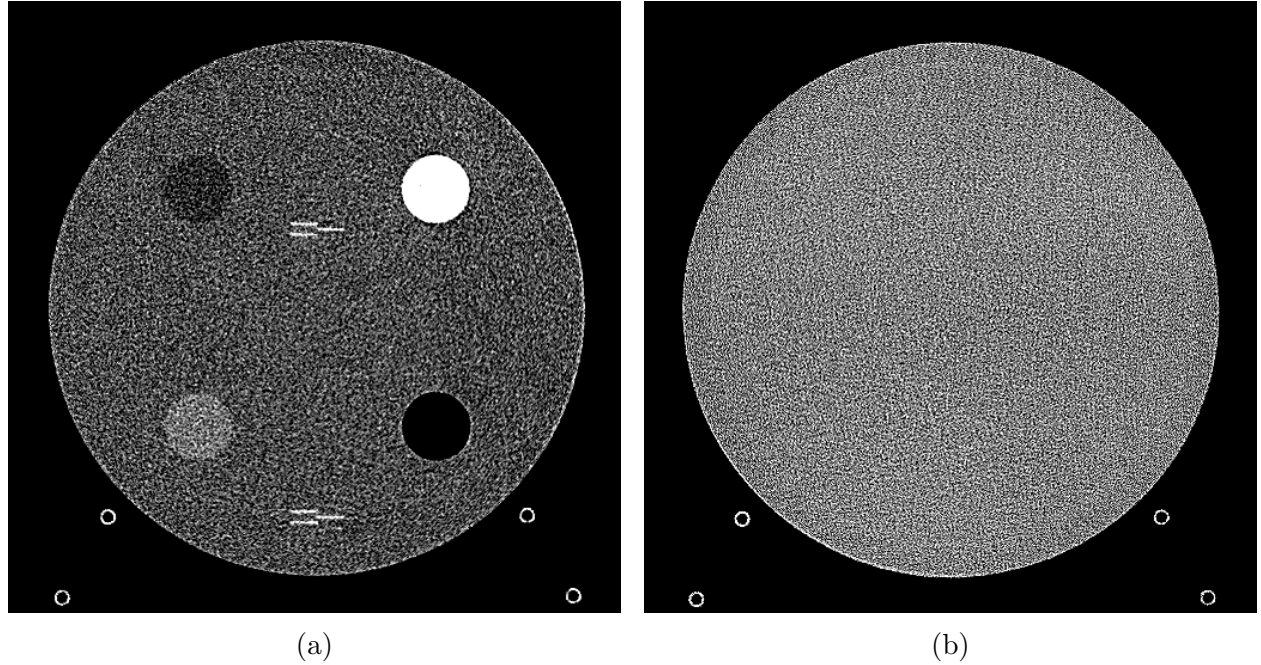


Figure 9: The ACR Phantom modules. (a) The phantom module 1 with 4 different inserts for CT number fidelity testing. In addition, two ramps of wires are visible near the phantom center. The image display window center is 150 HU and window width is 700 HU. (b) The phantom module 3 with a uniform water-like radiodensity of 0 HU. The display window center is 0 HU and window width is 400 HU.

channels, with a detector row spacing of 1.094 mm and a channel spacing of 0.054° . At the dual source mode, one detector of the scanner has 96 rows and 920 channels ($M_r = 96$, $M_c^1 = 920$), and the other detector has a smaller field-of-view with 96 rows and 640 channels ($M_c^2 = 640$). In addition, the two detectors have a z direction translation offset of 0.88 mm ($\Delta z_s^{1,2} = 0.88$ mm), and an angular offset of 95° in the X-Y plane ($\Delta\beta^{1,2} = 95^\circ$). Each source-detector pair has 9 possible focal spots and a CT scan can use any number of focal spots, depending on the scan protocol. In this paper, the exact displacement at each focal spot location, $(\Delta_u, \Delta_v, \Delta_z)$, is not disclosed as such information is confidential and protected by Siemens Healthineers.

To demonstrate the image quality, we first tested JENG’s performance on a standard CT phantom provided by the American College of Radiology (ACR), CT ACR 464 phantom³¹. Then we tested JENG on 7 clinical datasets, among which 5 are thoracic scans and 2 are pediatric head scans. The ACR 464 phantom contains four modules in total, with each module 40 mm in depth and 200 mm in diameter. The first module has 4 different inserts to test CT number fidelity and contains a series of wires for cross-plane resolution evaluation,

shown as white horizontal bars near the center in Fig. 9(a), and are visible in 0.5 mm z-axis increments. The second module tests low contrast resolution, but is not used in this paper. The third module, shown in Fig. 9(b), is a uniform cylinder with a radiodensity of water (0 HU) and is used to quantitatively measure CT number uniformity, image noise, and in-plane resolution. The fourth module consists of resolution bars of various spatial frequencies for further analysis on high contrast resolution. To scan the phantom, the scanner setup used dual sources with 2 focal spots at each source. In addition the projections were acquired at 100 KeV with a tube current of 718 mA and a helical pitch of 2.8.

For in-plane spatial resolution and artifacts analysis, we visually compared JENG against the state-of-the-art PWLS and FBP methods using the ACR phantom module 4, which has resolution bars of different spatial frequencies as mentioned before. Fig. 10 is an example transaxial image with resolution bars, with Figs. 10(a) reconstructed by PWLS from projections at a single source and 1 focal spot. Fig. 10(b) is JENG reconstructed from projections at a single source but with 2 flying focal spots. Fig. 10(c) is JENG at dual sources but with only 1 focal spot. Fig. 10(d) is JENG at dual sources and 2 flying focal spots. Each image has 8 bar patterns in the shape of squares, whose spatial frequencies from top going clockwise are 1.2, 1.0, 0.9, 0.8, 0.7, 0.6, 0.5 and 0.4 mm⁻¹. All images in Figs. 10 were reconstructed with an image sharpness similar to a Siemens BL-64 soft tissue high-contrast kernel, and with an image noise comparable to Siemens ADMIRE L1 denoising level.

The resolution bar visual comparison study, however, can be biased by observer subjectivity in some cases, and provides little information for system spatial resolution beyond a limiting value. Therefore, we also quantitatively evaluated JENG's in-plane resolution by using Modulation Transfer Function (MTF) for comparison between JENG and clinical-standard FBP. The MTF values for the FBP method is directly borrowed from a previous phantom study³². In addition, the noise variances for JENG and FBP reconstructions are matched to the same level for a fair comparison. To compute MTF, we calculated it in the same way as in citation³³ and the MTF computations source code can be downloaded at³⁴. In summary, the MTF analysis averaged all transaxial images in module 3, which is a uniform cylinder, into a 2D image, so that the imaging system was linear and spatially invariant. Then the MTF analysis computed the oversampled edge-spread-function for the generated 2D image, differentiated and Fourier transformed the edge-spread-function to the

frequency domain. The MTF is then the absolute value of the Fourier transform result.

For a more complete image analysis, we also measured the reconstruction noise profile through Noise Power Spectrum (NPS) and we visually compared the cross-plane spatial resolution between JENG and PWLS. The NPS computations followed the same procedures as in citation³³ with source code at³⁴. In summary, we selected multiple regions of interest in module 3. The regions of interest were all squares of the same size and had an average radiodensity of 0 HU. In addition, neighboring regions of interest overlapped with each other. Then, we performed a Fourier transform on each region of interest. The final NPS value equals to the ensemble average of the squared Fourier transform. For cross-plane resolution performance, we zoomed in on module 1’s series of wires from sagittal view, and visually compared wire pattern image sharpness of JENG and PWLS. For a fair cross-plane resolution comparison, all images have a matching noise variance in the uniform regions.

Finally, we tested JENG performance on 5 clinical thoracic scans and 2 pediatric head scan. The thoracic scans are public datasets from the AAPM Low-Dose Challenge, and were acquired from a single source Siemens Somatom Definition AS+ scanner with 736 detector channels, 64 detector rows and two focal spots. At the default focal spot, the source-to-isocenter distance, r_{so} , is 595 mm, and source-to-detector distance, r_{sd} is 1085.6 mm. The deflected focal spot has a displacement of $(\Delta_u = 0, \Delta_v = 5.45, \Delta_z = -0.66)$ mm, from the default to the deflected focal spot position. In addition, the deflected focal spot position has a source-to-isocenter distance, $r_{so} = 600.5$ mm, and a source-to-detector distance, $r_{sd} = 1091.0$ mm. The KVp for data acquisition was 100 KeV, tube current was 111 mA, the helical pitch was 0.6, and the number of projections per rotation was 1152. For comparison, JENG was compared to the clinical standard FBP reconstruction, which was provided for open access in the AAPM Low-Dose Challenge Competition and used a soft tissue Siemens kernel B-30f. We tuned the JENG reconstruction’s noise level to match that in FBP reconstruction. The pediatric head scan datasets were acquired at a major children’s hospital in the United States, and we compared brain soft tissues and bones between PWLS and JENG reconstructions. The CT scanner was Siemens Somatom Force in single source mode with 4 focal spots. The KVp for data acquisition was 100 KeV, tube current was 121 mA, the helical pitch was 0.55, and the number of projections per rotation was 1050. For a fair comparison, we tuned all head reconstructions’ image noise to be comparable to that for clinical standard reconstruction with a high contrast Siemens kernel HC-44s.

V. Results

V.A. ACR Phantom Study

Fig. 10 is PWLS and JENG reconstructions for the ACR phantom resolution bars. Fig. 10(a) is the PWLS image and is reconstructed from projections at a single X-ray source and a single focal spot. PWLS has no dual source or multiple focal spots reconstructions as PWLS is only applicable to single source single focal spot CT. Since the scan helical pitch is as high as 2.8, the PWLS image suffers from significant undersampling artifacts and insufficient projections, with a patchy mix of blacks and whites image appearance in Fig. 10(a) and blurry bar pattern in the magnified sub-figure. In contrast, Figs. 10(b), (c) and (d) are images reconstructed by JENG, with Fig. 10(b) at a single X-ray source but with dual focal spots, Fig. 10(c) at dual sources and a single focal spot, and Fig. 10(d) at dual sources and dual focal spots. Similar to PWLS, JENG at single X-ray source in Fig. 10(b) suffers from undersampling artifacts and low spatial resolution. At dual sources and a single focal spot in Fig. 10(c), JENG eliminates most of the undersampling artifacts from a high helical pitch, although the magnified sub-figure still has blurry details and has visible streaking aliasing artifacts near the phantom image peripheral regions. At dual sources and dual focal spots in Fig. 10(d), JENG effectively uses the native geometry and conjugate sets of projections from DS-FFS CT to overcome artifacts and reveal subtle image features. Consequently, Fig. 10(d) not only eliminates the patchy undersampling artifacts from a high helical pitch and significantly improves spatial resolution, but also suppresses the streaking aliasing artifacts.

Additionally, we also evaluated FBP's aliasing artifacts and spatial resolution in comparison to JENG. Fig. 11(a) is FBP's aliasing artifacts in a cropped region near the phantom periphery and is reconstructed with dual X-ray sources and dual focal spots. We observed that FBP's aliasing artifacts have a pattern of high density streaking and point along the direction of X-rays. In contrast, JENG in Fig. 11(b) has almost no aliasing artifacts, despite that a closer look reveals very faint and low density streaking along the path of X-rays. FBP's aliasing artifact pattern in the image periphery is consistent with Shannon-Nyquist sampling theorem, which concludes that FBP requires sufficient discrete projection data to inverse Fourier transform and interpolate projection data back to continuous image signals in the spatial domain. Since the phantom periphery receive fewer projections than those

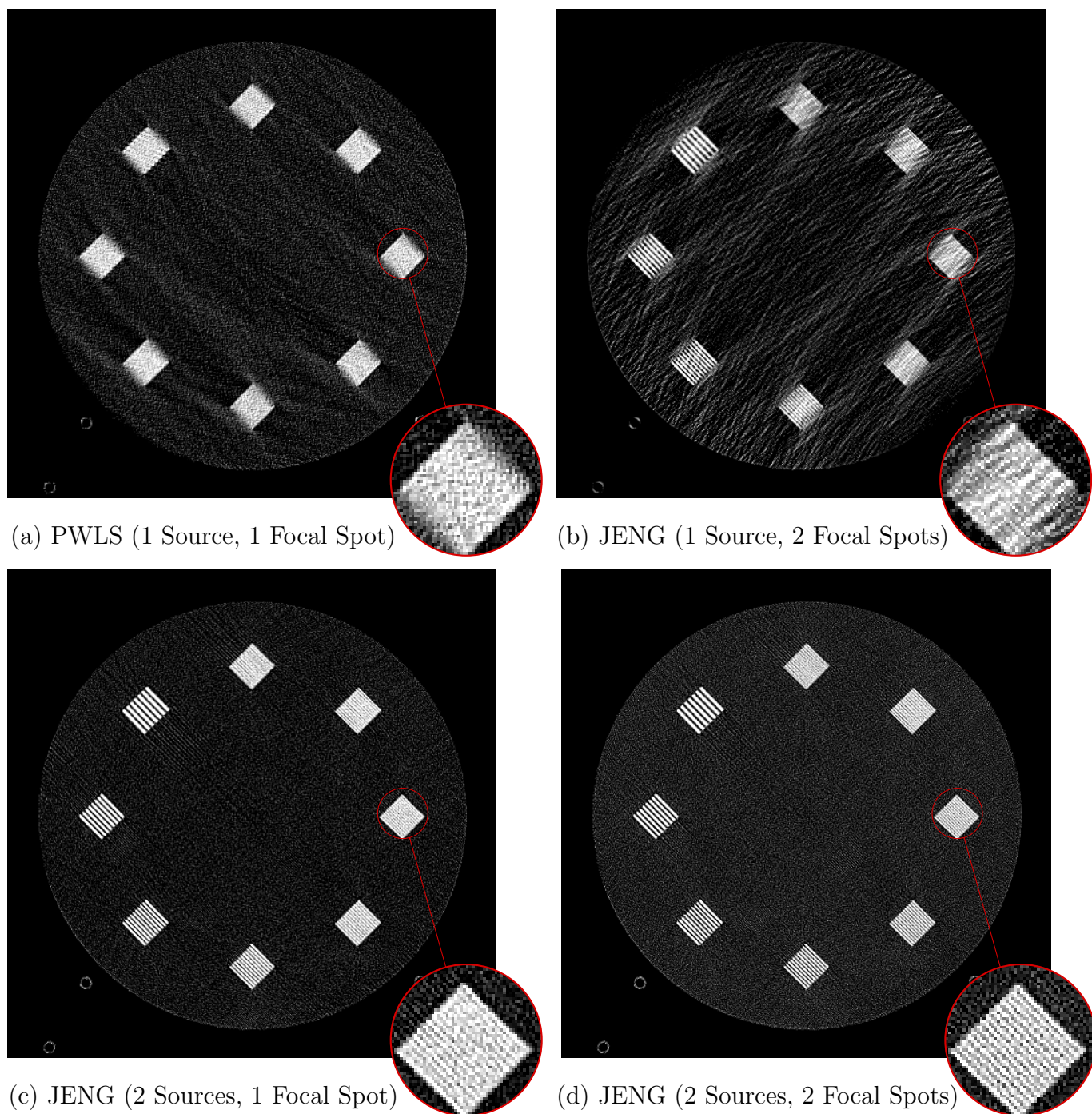


Figure 10: PWLS vs JENG performance, with a display window center of 650 HU and a window width of 1500 HU. The spatial frequency for bar patterns from top going clock-wise are 1.2, 1.0, 0.9, 0.8, 0.7, 0.6, 0.5, 0.4 mm^{-1} . (a) PWLS at single source, single focal spot with significant artifacts from a high helical pitch. (b) JENG at single source but with dual focal spots. (c) JENG at dual sources, single focal spot. (d) JENG at dual sources and dual focal spots. Note that JENG reconstruction in (d) have much clearer bar pattern and fewer artifacts than other images.

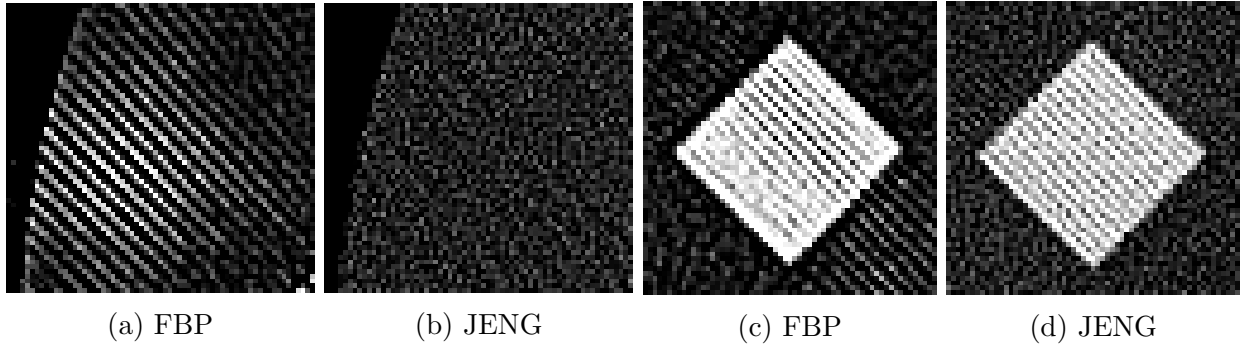


Figure 11: Aliasing artifacts and resolution bar comparison between FBP and JENG. (a) FBP aliasing artifacts with bright streaking pattern. (b) The same region reconstructed by JENG. Notice that the region shows almost no aliasing artifacts. (c) FBP resolution bar at 1.0 mm^{-1} . (d) JENG resolution bar at 1.0 mm^{-1} and the bar pattern is well resolved.

near the phantom center, FBP has insufficient discrete projections for data interpolation and shows more pronounced aliasing image artifacts near the image edge than the center⁹. JENG, however, is not based on Fourier transform and is not limited by Shannon-Nyquist Theorem. Therefore, JENG images are less susceptible to aliasing artifacts, leading to superior capability to suppress aliasing artifacts.

As to the spatial resolution comparison, Figs. 11(c) and (d) are FBP and JENG's resolution bars at spatial frequency 1.0 mm^{-1} . Since FBP has extensive amount of interpolation and geometry approximation, the FBP image has blurry and missing bar features. Meanwhile, JENG is based on linear algebra and accurate physics modeling with no interpolation and minimal geometry approximation. Consequently, JENG has a higher bar resolution than FBP and shows crisper image features. To corroborate with our visual assessment that JENG has a higher in-plane resolution than FBP, we compare the two algorithms' image sharpness quantitatively through MTF metrics in Fig. 12(a). We observe that the MTF for FBP drops to 0.1 at around 0.8 mm^{-1} , where an MTF of 0.1 is often considered the lowest contrast sensitivity for human visual observation. This observation aligns with our qualitative assessment in Fig. 11, which shows that bar patterns for FBP is unintelligible at a spatial frequency higher than 0.8 mm^{-1} . In contrast, JENG at both a single focal spot and dual focal spots have a higher MTF than FBP at all spatial frequencies, and their MTFs drop to 0.1 at around 1.1 mm^{-1} . Therefore, both qualitative and quantitative assessments have an agreed conclusion that JENG has a higher in-plane spatial resolution than FBP for the phantom study.

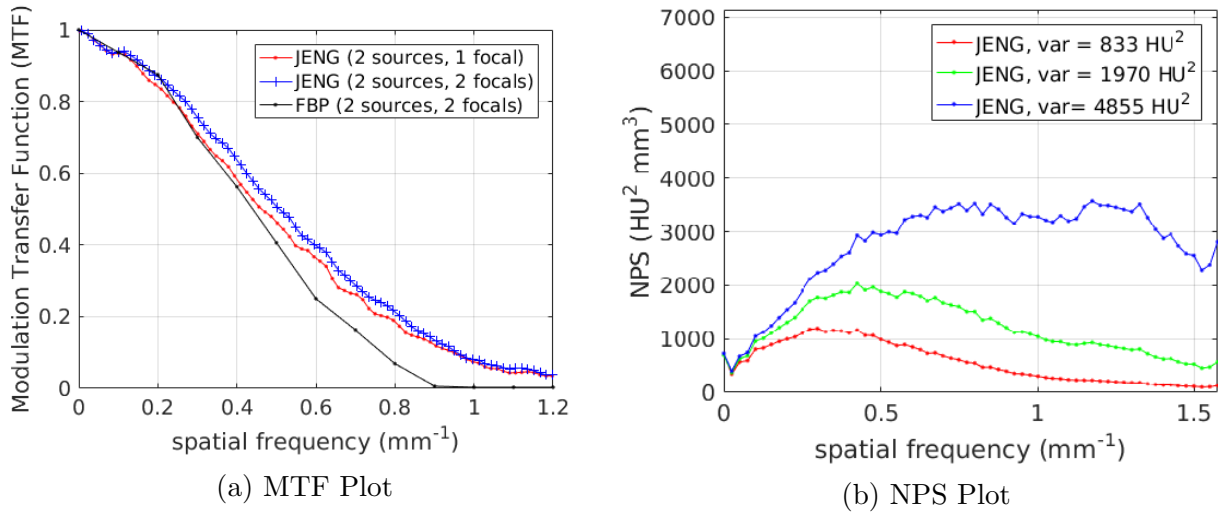


Figure 12: MTF and 3D NPS for FBP and JENG. (a) The MTF for FBP and JENG. Note that JENG has a higher MTF than FBP at all spatial frequencies. (b) The NPS for JENG at different noise levels. Note that a lower noise variance shifts JENG’s NPS peak towards a lower spatial frequency. This phenomenon indicates that a strong denoising for JENG can alter image noise texture.

The image noise profile is another topic of interest. Fig. 12(b) is the NPS for JENG at three noise levels with noise variances at 833 HU^2 , 1970 HU^2 and 4855 HU^2 . It is not surprising to observe that at all spatial frequencies JENG at higher noise variance has a larger NPS magnitude than that at lower noise variance. We also note that a lower noise variance shifts the NPS peak of JENG towards a lower spatial frequency, and this phenomenon indicates that a stronger denoising for JENG might alter the image noise texture. Furthermore, we observe that at an extremely low spatial frequency below 0.1 mm^{-1} , JENG retains moderate noise with an NPS magnitude at 750 HU^2 and fail to denoise further. To understand why JENG has limited success in denoising at a very low spatial frequency, we need to revisit JENG’s prior model, $R(X)$, in Eqn. (2). As explained before, $R(X)$ is a local-neighbor Markov Random Field, and denoise each voxel based on the voxel’s difference with its neighbors. The Markov Random Field prior model, however, is a low-pass filter. Therefore, $R(X)$ can suppress high-frequency noise well and preserve high-contrast image edges, but has limited success in low-frequency denoising and retains some very low frequency noise in the JENG images.

For many clinical applications, cross-plane resolution is equally important to in-plane resolution. To evaluate cross-plane resolution, we visually compared PWLS and JENG’s

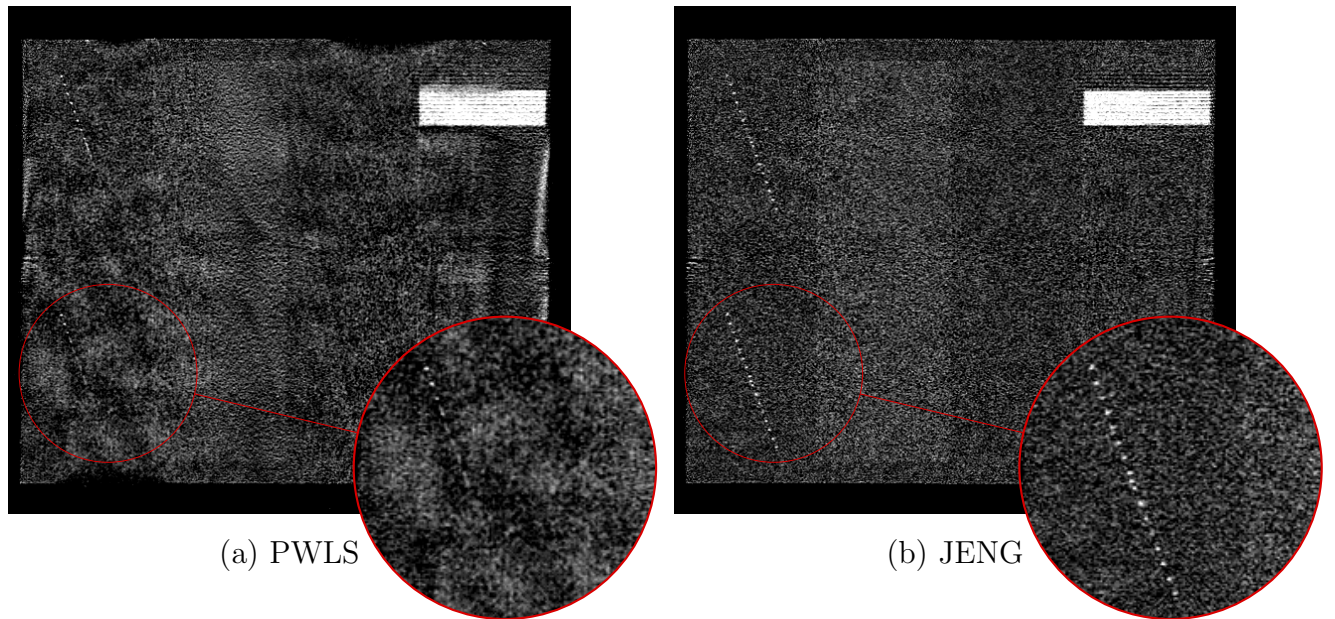


Figure 13: Cross-plane spatial resolution comparison between PWLS and JENG. (a) PWLS cross-plane image, with a display window center at 400 HU and a window width of 1200 HU. (b) The same region reconstructed by JENG. Note that all 17 wires are clearly visible in JENG’s magnified sub-figure, but are partially obscured in PWLS’s sub-figure.

wire series from sagittal view and the reconstructed images for PWLS and JENG have a matching noise variance in the phantom center. Figs. 13(a) and (b) are the phantom’s cross-plane sagittal view images, reconstructed by PWLS and JENG, respectively. In the cross-plane images, two ramps of wires in module 1 can be found on the left side of the images, with each ramp consisting of 17 wires and neighboring wires 0.5 mm apart from each other along the z axis. To better see the wire series, magnified sub-figures zoom in on a ramp of wires on the lower left corner of the images. We observe that all 17 wires in JENG’s cross-plane image are clearly visible. In contrast, PWLS has a lower cross-plane resolution and its image quality is undermined by undersampling artifacts because PWLS does not have a precise physics modeling for the DS-FFS CT native geometry and fails to utilize the conjugate sets of projections from the scanner for a higher resolution. Consequently, only 3 wires in PWLS images are visible and the rest are obscured by artifacts and noise.

V.B. Clinical Cases

None of the spatial resolution and artifact reduction advantages would hold unless JENG shows image quality improvement on clinical cases. To do so, we evaluated JENG on 5

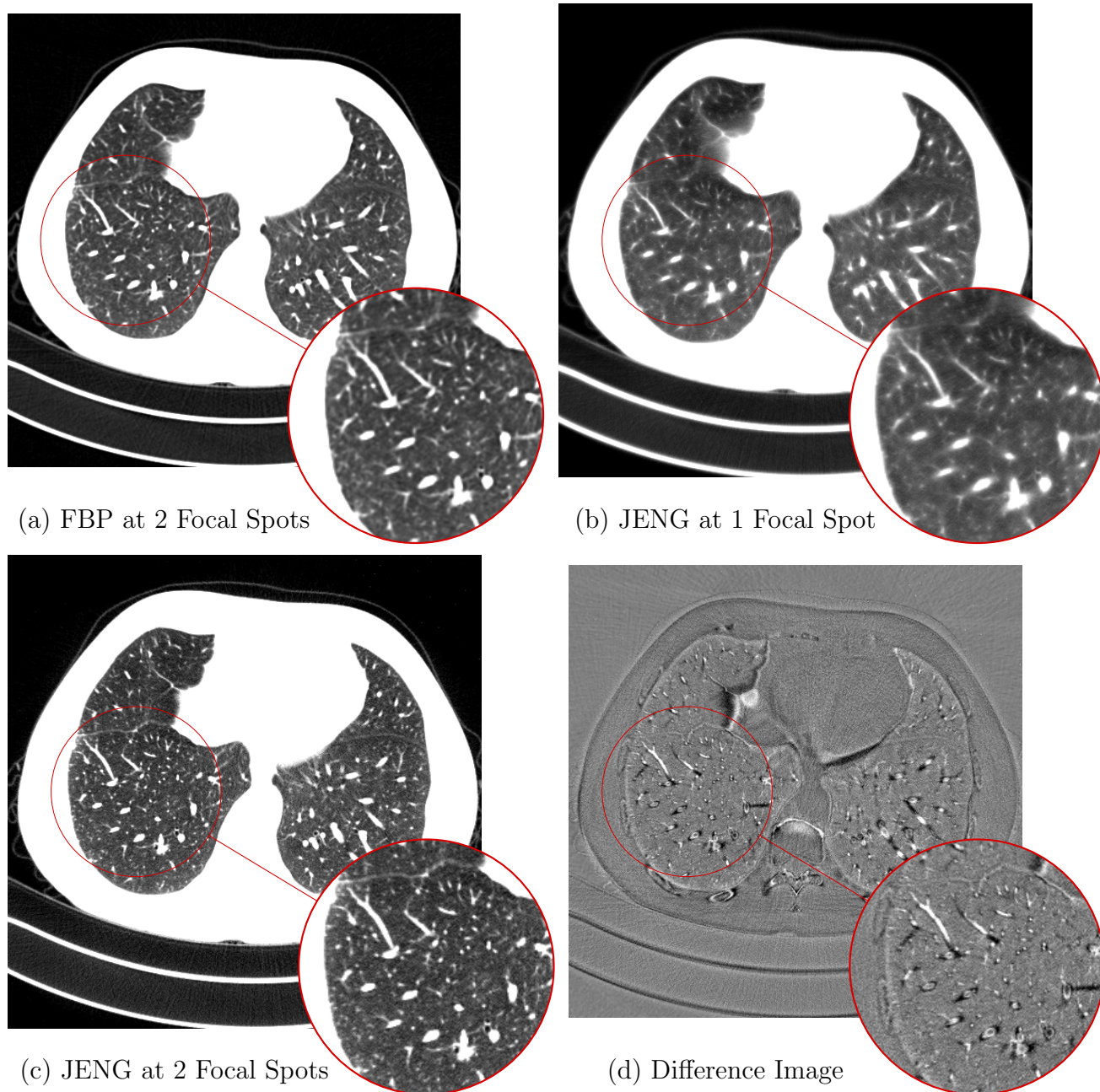


Figure 14: FBP and JENG image quality comparison at different numbers of focal spots. (a) An example FBP image from an AAPM Low Dose Challenge thoracic dataset. All images have a display window center at -750 HU and a window width of 500 HU. (b) The same image from JENG at a single focal spot. (c) JENG at dual focal spots. Note that JENG at dual focal spots has sharper image and shows a few image features that are missing in FBP. (d) The difference image between FBP and JENG at dual focal spots.

thoracic CT scans and 2 pediatric head scan datasets, and the exact experiment setup was discussed in Sec. IV..

Figs. 14(a) and (b) are an example transaxial image from a single source thoracic CT scan that has a helical pitch of 0.6 and 2 focal spots. Fig. 14(a) is the state-of-the-art clinical FBP image reconstructed from projections at both focal spots and was provided in the 2017 AAPM Low Dose Challenge Competition. Fig. 14(b) is the same image slice reconstructed by JENG, but was reconstructed by only 1 focal spot. Fig. 14(c) is JENG at 2 focal spots, and we note that JENG has clearer imaging than FBP for lung major fissures in both left and right lungs, whereas the left lung major fissure in FBP image is missing. In addition, JENG in Fig. 14(c) has sharper and much more details for lung vessels than FBP image in Fig. 14(a). To help readers better see the image quality difference between FBP and JENG, Fig. 14(d) shows the difference image between FBP and JENG at 2 focal spots, and shows that JENG has more and sharper image details than the state-of-the-art clinical FBP solution. Besides the findings above, Fig. 14(d) also shows that JENG has a better cardiac motion artifact reduction. This conclusion comes from the presence of dark shading in Fig. 14(d) near the atrium in the image center, where the FBP image shows cardiac motion artifacts but JENG eliminates most of the motion artifacts.

Fig. 15 shows an example axial image from a single source pediatric head scan dataset that has a helical pitch of 0.55 and 4 focal spots. Fig. 15(a) is PWLS at 1 focal spot, and Figs. 15(b) and (c) are JENG at 2 and 4 focal spots, respectively. Fig. 15(d) is the difference image between JENG at 4 focal spots and PWLS. A major advantage for JENG is its better detectability of small bone openings and a better aliasing artifacts reduction as we can observe in the magnified sub-figure of the difference image in Fig. 15(d). In comparison to JENG in Fig. 15(c), PWLS in Figs. 15(a) has more difficulty to distinguish image signals between small bone openings and the connecting bones and shows an inferior capability to suppress aliasing artifacts in the diagonal direction.

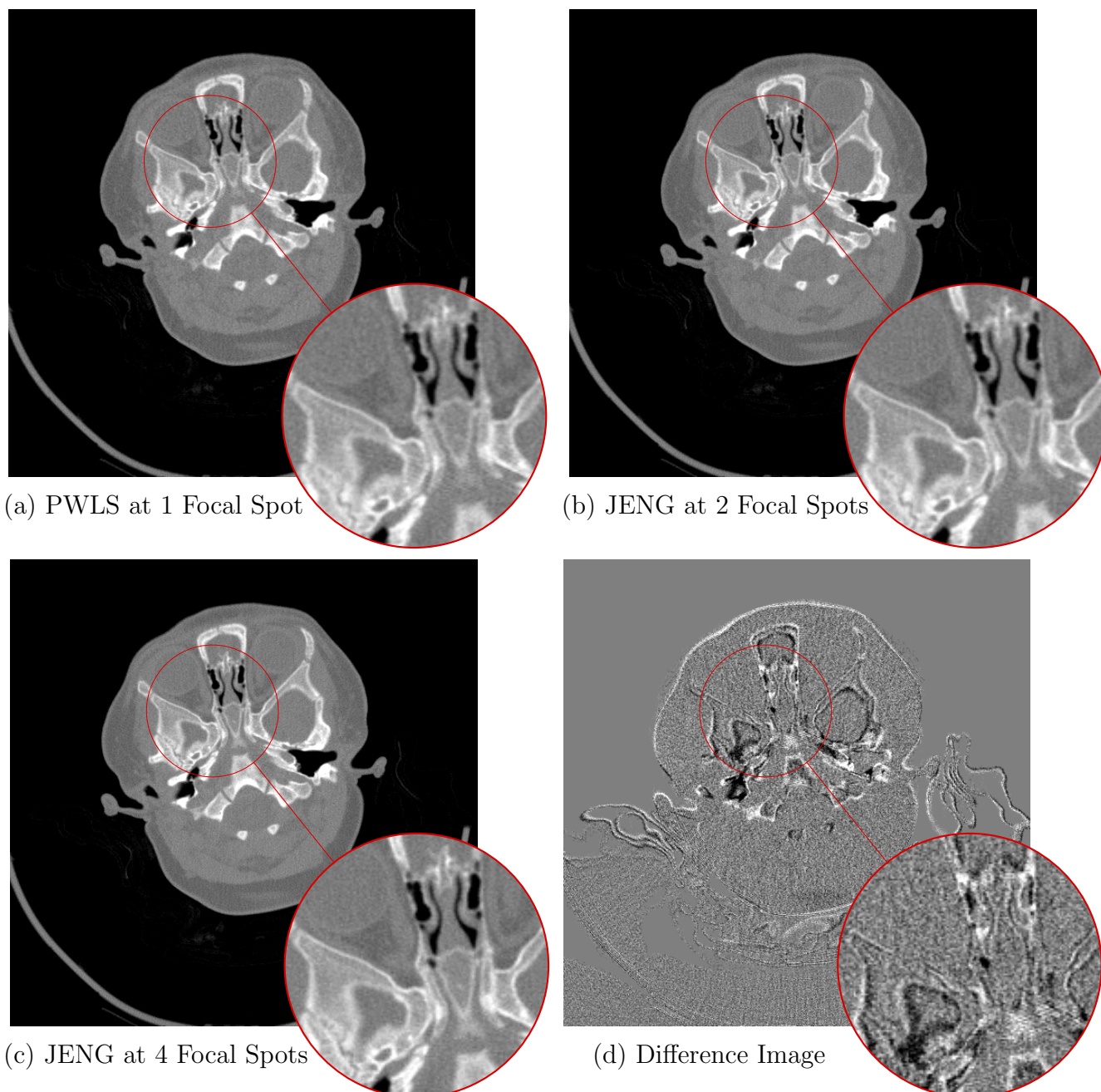


Figure 15: JENG reconstructed images at different numbers of focal spots. (a) An example image from PWLS head reconstruction. The image has a display window center of 35 HU and a window width of 1600 HU. (b) The same image slice from JENG at 2 focal spots. (c) JENG at 4 focal spots and has clearer bone openings and more image features for sinuses than PWLS. In addition, JENG has fewer aliasing artifacts. (d) The difference image between PWLS in (a) and JENG at 4 focal spots in (c).

VI. Discussion and Conclusion

Although the design purpose for DS-FFS CT is to minimize scan time by enabling a high helical pitch while simultaneously reducing undersampling artifacts, the FBP and PWLS reconstruction methods have not fully leveraged the physics and geometry for DS-FFS CT and have limited success in reducing undersampling artifacts. In addition, the projection data interpolation, rebinning and completion used by the FBP method may even cause a compromised spatial resolution when the pitch is high and cone angle is large. In response, we have presented the first physics based iterative reconstruction algorithm for DS-FFS CT and use the native cone-beam geometry and the precise dual source helical trajectory to achieve higher spatial resolution and eliminate more undersampling artifacts than existing methods. Experimental results on phantom and clinical datasets show that our new algorithm, JENG, has a Modulation Transfer Function 3.2 times higher than FBP methods at spatial frequency 0.8 mm^{-1} while significantly reducing undersampling artifacts in both FBP and PWLS images.

With a higher spatial resolution from JENG, radiologist can potentially better distinguish different objects or tissues located within a small proximity to each other. In the example of thoracic CT scans, JENG's improved image spatial resolution and contrast can lead to more accurate imaging on small indeterminate lung nodules and pulmonary emboli caused by intravascular disease. In the example of CT head scans, JENG's higher image resolution and contrast open the possibility to show crisper image details on temporal bones and minor skull fractures. In addition, given that undersampling artifacts are quantization artifacts caused by insufficient projections, JENG's capability to reduce the undersampling artifacts allows medical physicists to acquire fewer projections from patients without compromising image diagnostic values, and thereby lower radiation doses received by patients. Furthermore, since CT scan time is approximately proportional to the number of acquired projections, fewer acquired projections for JENG can significantly reduce the CT scan time and image temporal resolution is thereby higher.

Although JENG has many clinical implications discussed above, the NPS analysis shows that the existing implementation for JENG has an insufficient denoising capability at very low spatial frequency. Since the prior model for JENG is a Generalized Markov Random Field and is a low pass filter, JENG is successful in denoising high frequency content, but has

limited success at very low frequency. The relatively high NPS at very low spatial frequency ($<0.1 \text{ mm}^{-1}$), however, is unlikely to impair diagnostic values. Since image signals often have substantial energy at low frequencies but have much less energy at high frequencies, the Signal Noise Ratio (SNR) is high at low frequencies and image signals are readily apparent despite the noise. In contrast, the SNR is lower at high frequencies and a prior model with a good high frequency denoising, such as the Markov Random Field prior model, can significantly improve image quality. One adverse effect from a low pass filtering prior model is that the noise texture of JENG can appear different from that of FBP, and can negatively influence a radiologist's image perception if he is not used to the noise texture of JENG.

Another drawback in this paper's technical contribution is the lack of modeling on focal spot size and this paper assumes that the focal spot is a sizeless point. For most CT scans that require a high spatial resolution, the focal spot size is often less than 1 mm. In these applications, this paper's focal spot modeling as a sizeless point is a good assumption for high image quality. In a few other applications that require a large focal spot and reconstructions might benefit more from a precise focal spot size modeling, the sizeless point assumption can potentially lead to a loss of spatial resolution.

References

- ¹ M. Petersilka, H. Bruder, B. Krauss, K. Stierstorfer, and T. G. Flohr, Technical Principles of Dual Source CT, *European Journal of Radiology* **68**, 362–368 (2008).
 - ² R. V. Gottumukkala, M. K. Kalra, A. Tabari, A. Otrakji, and M. S. Gee, Advanced CT Techniques for Decreasing Radiation Dose, Reducing Sedation Requirements, and Optimizing Image Quality in Children, *Radiographics* **39**, 709–726 (2019).
 - ³ H. Turbell, *Cone-Beam Reconstruction Using Filtered Backprojection*, PhD thesis, Department of Electrical Engineering, Linkopings Universitet, Sweden, 2001.
 - ⁴ G. Wang, T. H. Lin, P. Cheng, and D. M. Shinozaki, A General Cone-Beam Reconstruction Algorithm, *IEEE Transactions on Medical Imaging* **12**, 486–496 (1993).
 - ⁵ F. Noo, M. Defrise, and R. Clackdoyle, Single-Slice Rebinning Method for Helical Cone-Beam CT, *Physics in Medicine & Biology* **44**, 561–570 (1999).
 - ⁶ M. Kachelriess, S. Schaller, and W. A. Kalender, Advanced Single-Slice Rebinning in Cone-Beam Spiral CT, *Medical Physics* **27**, 754–772 (2000).
 - ⁷ T. Flohr, K. Stierstorfer, S. Ulzheimer, H. Bruder, A. Primak, and C. McCollough, Image Reconstruction and Image Quality Evaluation for A 64-Slice CT Scanner with Z-Flying Focal Spot, *Medical Physics* **32** (2005).
 - ⁸ T. G. Flohr, H. Bruder, K. Stierstorfer, M. Petersilka, B. Schmidt, and C. H. McCollough, Image Reconstruction and Image Quality Evaluation for a Dual Source CT Scanner, *Medical Physics* **35**, 5882–5897 (2008).
 - ⁹ K. M. Brown and S. Žabic, Method for Reducing Windmill Artifacts in Multislice CT Images, *Proceedings of the SPIE* **7961**, 7961 – 7961 – 5 (2011).
 - ¹⁰ P. J. Pickhardt, M. G. Lubner, D. H. Kim, J. Tang, J. A. Ruma, A. M. D. Rio, and G. H. Chen, Abdominal CT With Model-Based Iterative Reconstruction (MBIR): Initial Results of A Prospective Trial Comparing Ultralow-Dose with Standard-Dose Imaging, *American Journal of Roentgenology* **199**, 1266–1274 (2012).
-

-
- ¹¹ J. B. Thibault, K. D. Sauer, C. A. Bouman, and J. Hsieh, A Three-Dimensional Statistical Approach to Improved Image Quality for Multi-Slice Helical CT, *Medical Physics* **34**(11) (2007).
- ¹² R. Zhang, J. B. Thibault, C. A. Bouman, K. D. Sauer, and J. Hsieh, Model-Based Iterative Reconstruction for Dual-Energy X-Ray CT Using a Joint Quadratic Likelihood Model, *IEEE Transactions on Medical Imaging* **33**, 117–134 (2014).
- ¹³ G. Widmann, D. D. Torre, R. Hoermann, P. Schullian, E. Gassner, R. Bale, and W. Puelacher, Ultralow-Dose Computed Tomography Imaging for Surgery of Midfacial and Orbital Fractures using ASIR and MBIR, *International Journal of Oral and Maxillofacial Surgery* **44**, 441 – 446 (2015).
- ¹⁴ X. Wang, A. Sabne, S. J. Kisner, A. Raghunathan, C. A. Bouman, and S. P. Midkiff, High Performance Model Based Image Reconstruction, *SIGPLAN Notice* **51**, 2:1–2:12 (2016).
- ¹⁵ J. Wang, T. Li, H. Lu, and Z. Liang, Penalized Weighted Least-Squares Approach to Sinogram noise Reduction and Image Reconstruction for Low-Dose X-ray Computed Tomography, *IEEE Transactions on Medical Imaging* **25**, 1272–1283 (2006).
- ¹⁶ V. Sridhar, X. Wang, P. Jin, and C. A. Bouman, Baseline MBIR Reconstruction For 2D and 3D Parallel-Beam CT, 2019, Download at <https://github.com/cabouman/OpenMBIR>.
- ¹⁷ J. A. Fessler, Michigan Image Reconstruction Toolbox, <http://web.eecs.umich.edu/~fessler/irt/irt/>, 2015.
- ¹⁸ X. Wang, V. Sridhar, Z. Ronaghi, R. Thomas, J. Deslippe, D. Dilworth, G. Buzzard, S. Midkiff, C. Bouman, and S. Warfield, Consensus Equilibrium Framework for Super-Resolution and Extreme-Scale CT Reconstruction, in *Proceedings of the International Conference for High Performance Computing, Networking, Storage and Analysis*, SC '19, New York, NY, USA, 2019, ACM.
- ¹⁹ Y. Kyriakou, M. Kachelrieß, M. Knaup, J. U. Krause, and W. A. Kalender, Impact of The Z-Flying Focal Spot on Resolution and Artifact Behavior for A 64-Slice Spiral CT Scanner, *European Radiology* **16**, 1206–1215 (2006).
-

-
- ²⁰ J. Zhao, Y. Lu, Y. Jin, E. Bai, and G. Wang, Feldkamp-Type Reconstruction Algorithms for Spiral Cone-Beam CT with Variable Pitch, *Journal of X-Ray Science and Technology* **15**, 177–196 (2007).
- ²¹ T. G. Flohr, S. Leng, L. Yu, T. Aiemendinger, H. Bruder, M. Petersilka, C. D. Eusemann, K. Stierstorfer, B. Schmidt, and C. H. McCollough, Dual-Source Spiral CT with Pitch up to 3.2 and 75 ms Temporal Resolution: Image Reconstruction and Assessment of Image Quality, *Medical Physics* **36**, 5641–5653 (2009).
- ²² K. Sauer and C. Bouman, A Local Update Strategy for Iterative Reconstruction from Projections, *IEEE Transactions on Signal Processing* **41**(2) (1993).
- ²³ A. Sabne, X. Wang, S. J. Kisner, C. A. Bouman, A. Raghunathan, and S. P. Midkiff, Model-Based Iterative CT Image Reconstruction on GPUs, in *Proceedings of the 22Nd ACM SIGPLAN Symposium on Principles and Practice of Parallel Programming*, PPOPP '17, pages 207–220, New York, NY, USA, 2017, ACM.
- ²⁴ X. Wang, A. Sabne, P. Sakdhnagool, S. J. Kisner, C. A. Bouman, and S. P. Midkiff, Massively Parallel 3D Image Reconstruction, in *Proceedings of the International Conference for High Performance Computing, Networking, Storage and Analysis*, SC '17, pages 3:1–3:12, New York, NY, USA, 2017, ACM.
- ²⁵ J. R. Shewchuk, *An Introduction to the Conjugate Gradient Method Without the Agonizing Pain*, Carnegie Mellon University, Pittsburgh, PA, 1994.
- ²⁶ H. Erdogan and J. Fessler, Ordered Subsets Algorithms for Transmission Tomography, *Phys. Med. Biol.* **44**(11) (1999).
- ²⁷ S. Ahn and J. A. Fessler, Globally Convergent Image Reconstruction for Emission Tomography Using Relaxed Ordered Subsets Algorithms, *IEEE Transactions on Medical Imaging* **22**, 613–626 (2003).
- ²⁸ J. Qi and R. H. Huesman, Effect of Errors in The System Matrix on Maximum A Posteriori Image Reconstruction, *Physics in Medicine & Biology* **50**, 3297–3312 (2005).
- ²⁹ G. T. Buzzard, S. H. Chan, and C. A. Bouman, Plug-and-Play Unplugged: Optimization Free Reconstruction using Consensus Equilibrium, ArXiv e-prints (2017).
-

-
- ³⁰ V. Sridhar, X. Wang, G. T. Buzzard, and C. A. Bouman, Distributed Iterative CT Reconstruction using Multi-Agent Consensus Equilibrium, arXiv Preprint (2019), arXiv:1911.09278 (eess).
- ³¹ T. A. C. of Radiology, American College of Radiology CT Accreditation Program Testing Instructions, <https://www.acraccreditation.org/~media/ACRAccreditation/Documents/CT/CT-Accreditation-Testing-Instructions.pdf>, 2019.
- ³² J. Solomon, A. Mileto, J. C. Ramirez-Giraldo, and E. Samei, Diagnostic Performance of an Advanced Modeled Iterative Reconstruction Algorithm for Low-Contrast Detectability with a Third-Generation Dual-Source Multidetector CT Scanner: Potential for Radiation Dose Reduction in a Multireader Study, *Radiology* **275**, 735–745 (2015).
- ³³ S. N. Friedman, G. S. Fung, J. H. Siewerdsen, and B. M. Tsui, A Simple Approach to Measure Computed Tomography (CT) Modulation Transfer Function (MTF) and Noise-Power Spectrum (NPS) Using The American College of Radiology (ACR) Accreditation Phantom, *Medical Physics* **40**, 051907 (2013).
- ³⁴ S. N. Friedman, Calculation of CT MTF and NPS Using The ACR Accreditation Phantom, <https://www.mathworks.com/matlabcentral/fileexchange/41401-calculation-of-ct-mtf-and-nps-using-the-acr-accreditation-phantom>, 2020.
-